iScience

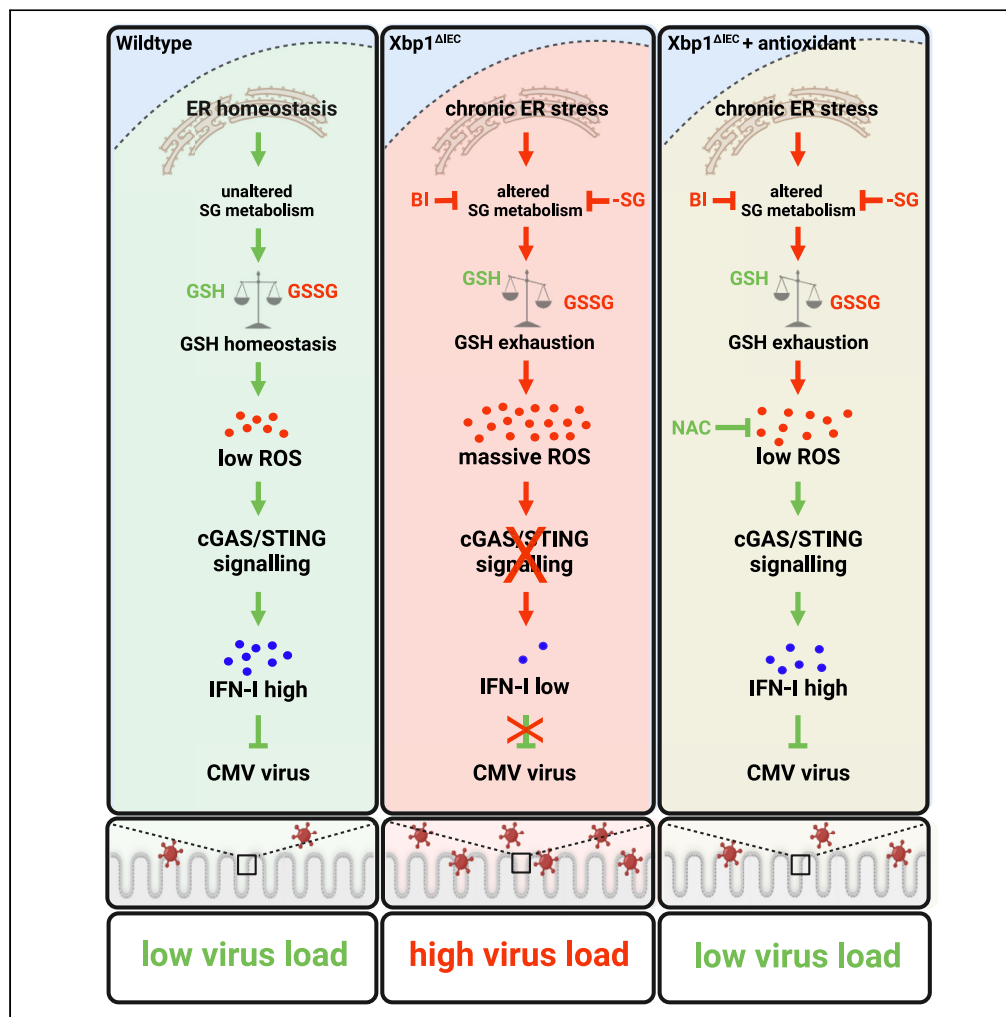**Article**

Serine metabolism is crucial for cGAS-STING signaling and viral defense control in the gut

Björn Becker, Felix Wottawa, Mohamed Bakr, ..., Philip Rosenstiel, Johannes Meiser, Konrad Aden

p.rosenstiel@mucosa.de (P.R.)
Johannes.meiser@lih.lu (J.M.)
k.aden@ikmb.uni-kiel.de (K.A.)

Highlights

ER stress reprograms serine and 1C metabolism to promote GSH supply in IECs

ER stress abrogates cGAS/STING signaling via the accumulation of ROS

Antioxidant therapy restores virus defense control in ER-stressed IECs

ER stress-mediated rewiring of serine metabolism is a key molecular feature in IBD

Article

Serine metabolism is crucial for cGAS-STING signaling and viral defense control in the gut

Björn Becker,[1,15] Felix Wottawa,[2,15] Mohamed Bakr,[2,15] Eric Koncina,[3] Lisa Mayr,[4] Julia Kugler,[2] Guang Yang,[2] Samuel J. Windross,[5] Laura Neises,[1] Neha Mishra,[2] Danielle Harris,[2] Florian Tran,[2,14] Lina Welz,[2,14] Julian Schwärzler,[4] Zoltán Bánki,[6] Stephanie T. Stengel,[2] Go Ito,[7] Christina Krötz,[1] Olivia I. Coleman,[8] Christian Jaeger,[9] Dirk Haller,[8,10] Søren R. Paludan,[5] Richard Blumberg,[11] Arthur Kaser,[12] Luka Cicin-Sain,[13] Stefan Schreiber,[2,14] Timon E. Adolph,[4] Elisabeth Letellier,[3] Philip Rosenstiel,[2,*] Johannes Meiser,[1,*] and Konrad Aden[2,14,16,*]

SUMMARY

Inflammatory bowel diseases are characterized by the chronic relapsing inflammation of the gastrointestinal tract. While the molecular causality between endoplasmic reticulum (ER) stress and intestinal inflammation is widely accepted, the metabolic consequences of chronic ER stress on the pathophysiology of IBD remain unclear. By using *in vitro*, *in vivo* models, and patient datasets, we identified a distinct polarization of the mitochondrial one-carbon metabolism and a fine-tuning of the amino acid uptake in intestinal epithelial cells tailored to support GSH and NADPH metabolism upon ER stress. This metabolic phenotype strongly correlates with IBD severity and therapy response. Mechanistically, we uncover that both chronic ER stress and serine limitation disrupt cGAS-STING signaling, impairing the epithelial response against viral and bacterial infection and fueling experimental enteritis. Consequently, the antioxidant treatment restores STING function and virus control. Collectively, our data highlight the importance of serine metabolism to allow proper cGAS-STING signaling and innate immune responses upon gut inflammation.

INTRODUCTION

Inflammatory bowel diseases (IBD), classically divided into ulcerative colitis (UC) and Crohn's disease (CD), describe a group of chronic disorders defined by relapsing and remitting episodes of gastrointestinal inflammation. Although the introduction of the targeted inhibition of pro-inflammatory pathways (e.g., anti-TNF, anti-IL12/23) has significantly improved patient care, disease-associated complications such as IBD-related hospitalizations and surgery still contribute to the major socioeconomic burden of IBD.[1] In the past years, IBD-related cytomegalovirus (CMV) infections have seen a steep rise and increase the risk of hospitalization and proctocolectomy.[2,3]

Several studies have already demonstrated that the deregulation of ER stress signaling pathways in intestinal epithelial cells (IECs) is linked to IBD initiation and progression.[4–8] ER stress describes a state of disrupted cellular homeostasis, which occurs when the balance between ER-folding capacity and protein load is disturbed.[9,10] Thereby, the consequences of ER stress on intestinal homeostasis appear to be multifaceted, ranging from impaired mucosal barrier function to altered intestinal microbial composition to uncontrolled immune responses.[11–13] Especially, IECs with a high secretory demand such as Paneth and Goblet cells are highly susceptible to changes in ER homeostasis.[7,8] Ultimately, ER stress triggers a detrimental inflammatory reaction that drives mucosal tissue damage in human patients with IBD.[14,15] Usually, to restore ER homeostasis, cells activate the unfolded protein response (UPR), which consists of three major pathways (specifically,

[1]Luxembourg Institute of Health, Department of Cancer Research, Luxembourg, Luxembourg
[2]Institute of Clinical Molecular Biology, Christian-Albrechts-University and University Hospital Schleswig-Holstein, Campus Kiel, 24105 Kiel, Germany
[3]Faculty of Science, Technology and Medicine, Department of Life Sciences and Medicine, Université du Luxembourg, Luxembourg, Luxembourg
[4]Department of Internal Medicine I, Gastroenterology, Hepatology, Metabolism & Endocrinology, Medical University of Innsbruck, Innsbruck, Austria
[5]Department of Biomedicine, Aarhus University, Aarhus, Denmark
[6]Institute of Virology, Department of Hygiene, Microbiology and Public Health, Medical University of Innsbruck, Innsbruck, Austria
[7]Department of Gastroenterology and Hepatology, Tokyo Medical and Dental University, Tokyo, Japan
[8]Chair of Nutrition and Immunology, TUM School of Life Sciences, Technical University of Munich, Luxembourg, Luxembourg
[9]Luxembourg Centre for Systems Biomedicine, University of Luxembourg, Esch-sur-Alzette, Luxembourg
[10]ZIEL-Institute for Food & Health, Technical University of Munich, 85354 Freising, Germany
[11]Gastroenterology Division, Department of Medicine, Brigham and Women's Hospital, Harvard Medical School, Boston, MA, USA
[12]Division of Gastroenterology and Hepatology, Department of Medicine, Addenbrooke's Hospital, University of Cambridge, Cambridge, England, UK
[13]Helmholtz Zentrum für Infektionsforschung, Braunschweig, Germany
[14]Department of Internal Medicine I, Christian-Albrechts-University and University Hospital Schleswig-Holstein, Campus Kiel, 24105 Kiel, Germany
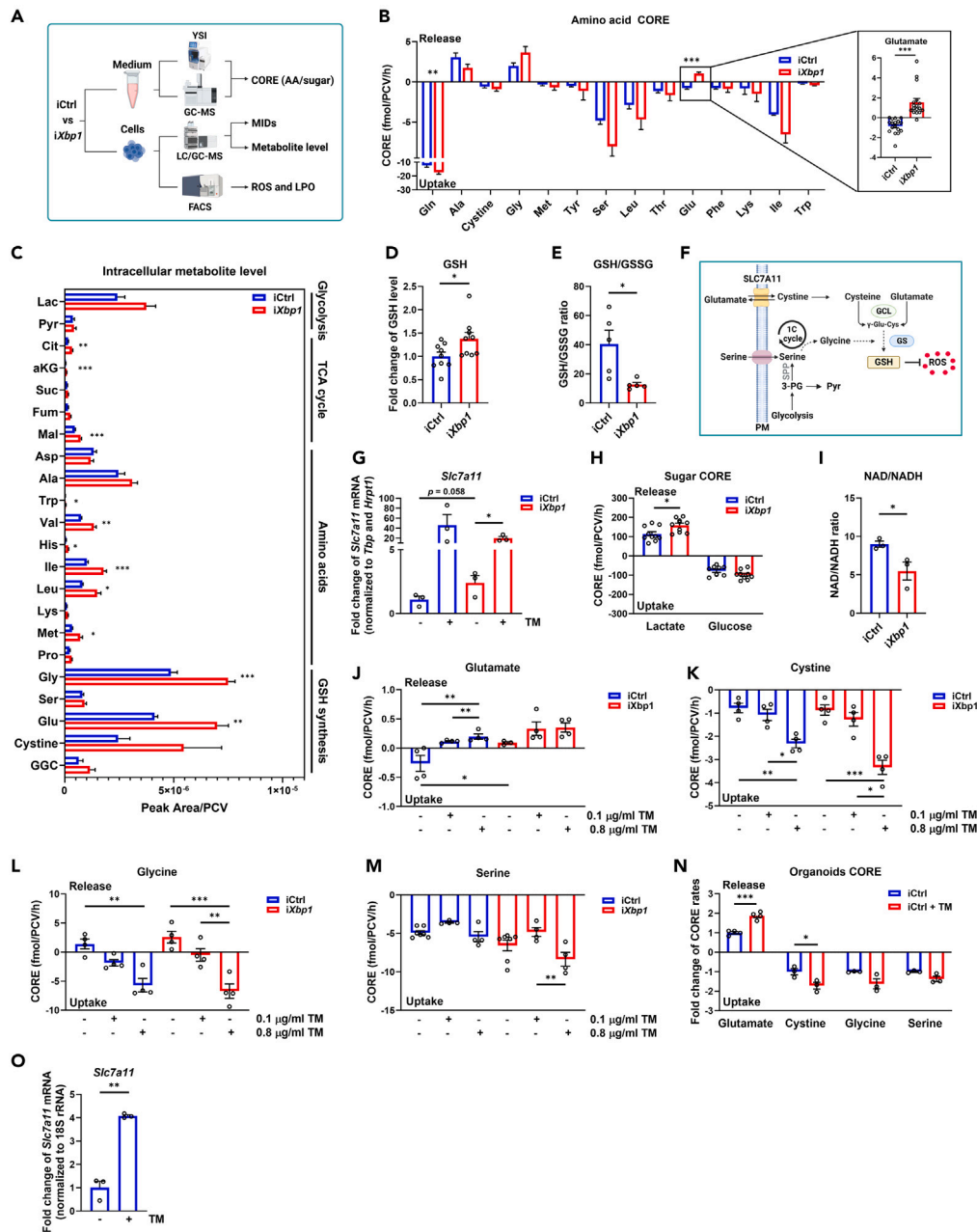[15]These authors contributed equally
[16]Lead contact
*Correspondence: p.rosenstiel@mucosa.de (P.R.), Johannes.meiser@lih.lu (J.M.), k.aden@ikmb.uni-kiel.de (K.A.)
https://doi.org/10.1016/j.isci.2024.109173

Figure 1. ER stress induces a distinct ROS-dependent metabolic reprogramming of the amino acid metabolism to support GSH synthesis in IECs

(A) Schematic overview of the experimental workflow used to analyze metabolic and cellular changes in wild-type (iCtrl) and chronically ER-stressed (iXbp1) Mode-K cells.

(B) *In vitro* uptake rates of amino acids (left) and zoom-in of glutamate (right). Absolute consumption and release rates (CORE) in fmol/PCV/h are displayed (n ≥ 3).

(C) Intracellular metabolite level (peak area/PCV) in iCtrl and iXbp1 cells (n ≥ 3).

(D) Intracellular GSH level in iCtrl and iXbp1 cells (n = 9, paired t-test).

(E) GSH/GSSG ratios in iCtrl and iXbp1 cells (n = 3, paired t-test).

(F) Schematic illustration of the GSH synthesis pathway. (GCL: glutamate-cysteine ligase; GS: glutathione synthetase, SSP: serine *de novo* synthesis pathway; PM: plasma membrane).

(G) *Slc7a11* mRNA expression in iCtrl and iXbp1 cells treated with (+) or without (−) TM (n = 3).

(H) Absolute CORE rates in fmol/PCV/h of glucose and lactate in iCtrl (n = 10) and iXbp1 cells (n = 9).

(I) NAD/NADH ratio in iCtrl and iXbp1 cells (n = 3).

(J–M) Absolute CORE rates of (J) glutamate, (K) cysteine, (L) glycine, and (M) serine in iCtrl and iXbp1 cells in response to TM treatment (n = 4, two-way ANOVA).

Figure 1. Continued

(N) Absolute CORE rates of the indicated amino acids in murine SI organoids cultures (derived from *Xbp1*fl/fl mice) in the presence or absence of 0.1 µg/mL TM. Representative experiment is shown.

(O) *Slc7a11* mRNA expression in murine SI organoids (derived from *Xbp1*fl/fl mice) treated with (+) or without (−) 0.1 µg/mL TM (n = 3, paired t-test). *p < 0.05, **p < 0.01, ***p < 0.001.

the IRE1/XBP1-, PERK/ATF4-, and ATF6-pathway).[9] Single-nucleotide polymorphisms (SNPs) in *X-box binding protein 1* (*XBP1*) cause an ER stress sensitive variant resulting in increased IBD susceptibility and intestinal tumorigenesis.[16,17]

In contrast to the pathophysiological consequences, the metabolic consequences of impaired ER homeostasis in the context of IBD remain largely unattended. Besides the clearance of misfolded proteins, ER-stressed cells have to reprogram their metabolism to handle the increased oxidative burden. For instance, cells can maximize the metabolic output toward reduction/oxidation (RedOx) control by utilising available carbon sources differently. In this regards, the serine and one-carbon (1C) metabolism are of great importance to provide the building block glycine for the synthesis of the most abundant antioxidant glutathione (GSH).[18] Since GSH synthesis also requires the amino acids cysteine and glutamate, cells need to additionally fine-tune the availability of these amino acids.[19] Importantly, a prolonged disequilibrium of the RedOx homeostasis is one of the notorious features of patients suffering from chronic inflammatory disease.[20,21]

Another important aspect is the association between impaired RedOx homeostasis and increased lipid peroxidation (LPO).[22] Recent studies indicate that by-products of LPO reactions (e.g., 4-HNE) interfere with the activation of the cGAS-STING pathway.[23] In general, this pathway allows the initiation of the host defense against pathogens by directly sensing cytosolic double-stranded DNA (dsDNA) derived from viruses (e.g., CMV) or cyclic dinucleotides derived from intracellular bacteria (e.g., *Listeria monocytogenes*).[24–26] After binding of cytosolic dsDNA and subsequent cGAMP production by cGAS, STING is activated and transported from the ER through the ER-Golgi intermediate compartment (ERGIC) into the Golgi apparatus. Here, STING recruits Tank-binding kinase 1 (TBK1) and interferon regulatory factor 3 (IRF3), controlling type-I IFN (e.g., IFN-β) production and secretion. IFN-β then induces a variety of antiviral, immunomodulatory, or anti-proliferative interferon-stimulated genes (ISGs) such as *CXCL10*.[26] As such, cGAS-STING signaling is critically involved in type-I IFN induction during CMV infection, and CMV actively antagonizes STING-mediated IFN induction, highlighting the potential role of STING as a crucial first line of defense against CMV infection.[27–29] Interestingly, meta-analyses of retrospective clinical data of patients with IBD indicate that the disease extent and disease severity directly correlate with CMV colitis risk. However, the underlying molecular mechanisms that drive susceptibility to CMV infection in patients with IBD remain enigmatic.[3] Due to its localization as an ER-resident protein, it is postulated that STING function is closely intertwined with ER homeostasis. However, to what extent disturbance of the UPR directly affects cGAS-STING-sensing is not known. Several studies support the notion that ER stress is an important upstream modulator of STING activity in response to PAMPs and DAMPs[30,31] and pro-regenerative IL-22 signaling.[32]

In this study, we combined metabolic profiling with transcriptome analyses of IBD cohorts and discovered a distinct metabolic reprogramming toward GSH metabolism in the intestinal epithelium upon chronic ER stress. This metabolic phenotype correlates with IBD severity and therapy-response status. Despite the metabolic rewiring toward RedOx control, ER-stressed IECs show an imbalanced RedOx homeostasis suppressing the initiation of cGAS-STING signaling in response to invading viruses and bacteria. Using pharmacological interventions, we further underpinned the essential role of the serine metabolism regarding cGAS-STING signaling in chronic ER stress. Our findings therefore shed new lights on the underlying mechanisms driving the increased susceptibility of patients with IBD against CMV infections.

RESULTS

Chronic endoplasmic reticulum stress promotes glutathione synthesis by adapting amino acid uptake in intestinal epithelial cells

Unresolved ER stress represents a critical hallmark of chronic intestinal inflammation and contributes to the pathogenesis of IBD.[12,33] As such, defects in components of the UPR machinery are linked to IBD development.[7,34,35] Since the loss of the IBD risk gene *XBP1/Xbp1* causes ER stress and drives intestinal inflammation in mice and humans,[7] we studied the metabolic consequences of Xbp1 deficiency in IECs (i*Xbp1*) by using different metabolic read-outs (Figure 1A).

While ^{13}C flux analysis did not reveal striking differences in the central carbon metabolism of chronically ER-stressed IECs (Figures S1A–S1D), exchange rates of distinct amino acids were heavily altered. Xbp1 loss results in increased glutamine consumption and a striking switch from glutamate consumption toward glutamate release. Additionally, we also observed a general trend toward increased amino acid uptake under *Xbp1* deficiency (Figure 1B). Intracellular metabolic steady-state levels of various metabolites including different amino acids and TCA cycle intermediates were elevated. Most consistently, i*Xbp1* cells showed a strong increase in metabolites related to GSH (GSH) synthesis, such as glycine, glutamate, and cystine (Figure 1C). In line with this notion, intracellular GSH level were increased in i*Xbp1* cells (Figure 1D). Since the primordial function of GSH is to counterbalance free ROS-derived radicals, the reduced GSH over GSSG ratio suggests an unbalanced RedOx homeostasis under *Xbp1*-deficiency (Figure 1E). Additionally, cells can increase intracellular cysteine availability via the cystine/glutamate antiporter Slc7a11 to support GSH synthesis[36] (Figure 1F). In line with this, we observed *Slc7a11* upregulation in response to ER stress (Figure 1G). Moreover, i*Xbp1* cells released more lactate and showed a reduced NAD/NADH ratio compared to their wild-type counterparts (iCtrl) (Figures 1H and 1I). Overall, the results indicate a metabolic plasticity toward GSH metabolism to counterbalance reactive oxygen species (ROS).
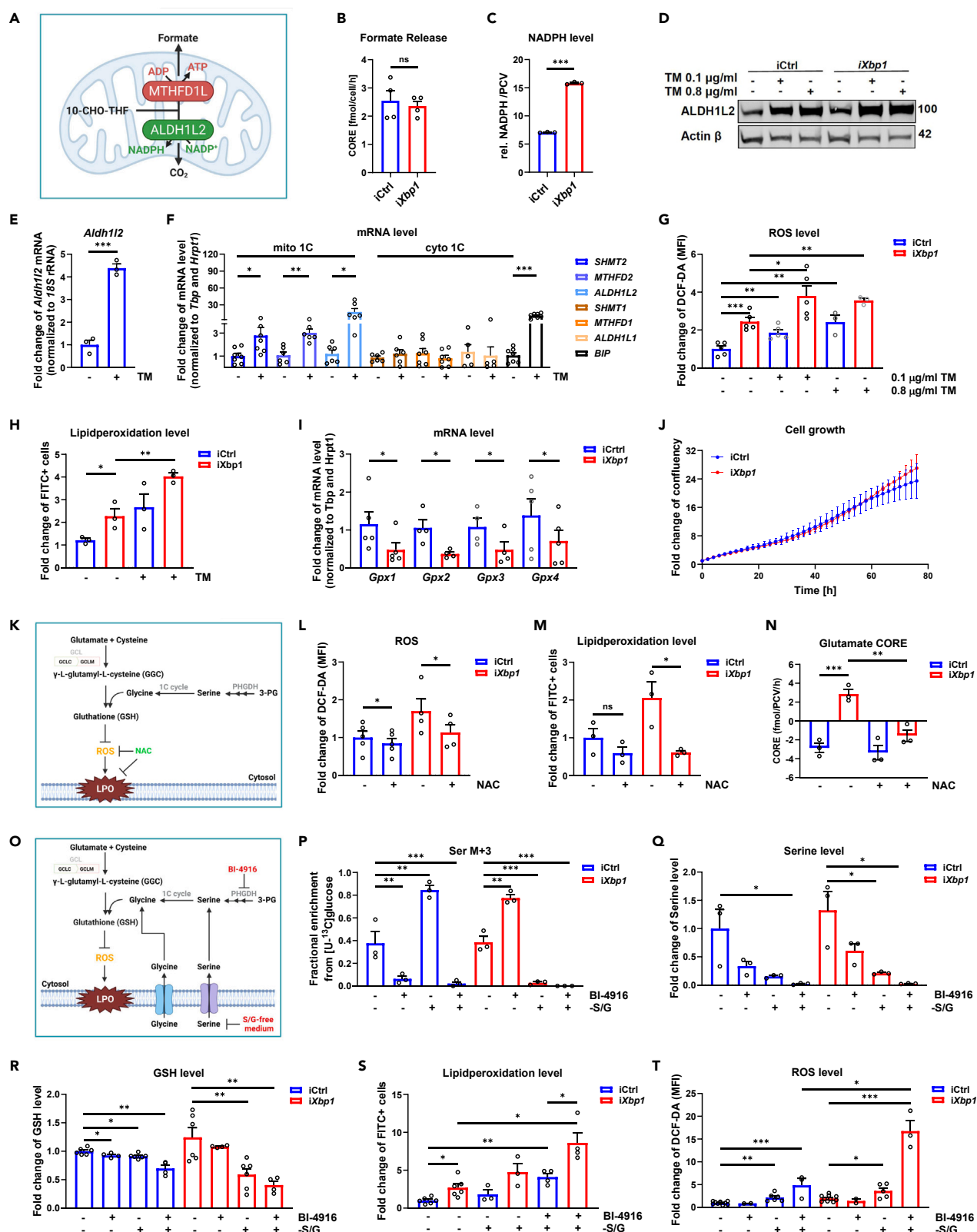
Figure 2. IECs activates the mitochondrial arm of the 1C cycle to counterbalance ER stress-induced RedOx imbalance by boosting GSH and NADPH synthesis

(A) Schematic illustration of the 10-Formyl-Tetrahydrofolate (10-F-THF) branching point in the mitochondrial 1C metabolism.

(B) Absolute formate release rates (fmol/PCV/h) in iCtrl and i*Xbp1* cells (n = 4).

(C) Relative NADPH level of iCtrl and i*Xbp1* cells (n = 3).

(D) ALDH1L2 expression level in iCtrl and i*Xbp1* cells in the presence (+) and absence (−) of TM. VINCULIN serves as loading control.

(E) *Aldh1l2* gene expression in murine SI organoids (derived from *Xbp1*$^{fl/fl}$ mice) treated with 0.8 µg/mL TM for 24h (n = 3).

(F) Relative mRNA expression level of mitochondrial (mito 1C) and cytoplasmic (cyto 1C) enzymes of the 1C cycle in wild-type Mode-K cells (iCtrl) treated with or without 0.8 µg/mL TM for 24h. ER chaperone *Bip/Grp78* serves as a positive control for ER stress induction.

(G) Relative cytoplasmic ROS levels of iCtrl and i*Xbp1* cells treated with or without TM for 24h (n ≥ 3).

(H) Relative percentage of FITC$^+$ cells in iCtrl and i*Xbp1* cells treated with 0.1 µg/mL TM for 24h (n = 3).

(I) Relative mRNA expression level of the indicated Gpx genes in iCtrl and i*Xbp1* cells (n = 4, paired t-test).

(J) Growth curve of iCtrl and i*Xbp1* cells (n = 3).

(K). Schematic diagram of the antioxidant treatment strategy to reduce intracellular ROS level.

(L) Relative cytoplasmic ROS level of NAC-treated iCtrl and i*Xbp1* cells (n ≥ 4, paired t-test).

(M) Relative percentage of FITC$^+$ cells in iCtrl and i*Xbp1* cells after 24h NAC treatment (n = 3, paired t-test).

(N) Absolute consumption and release rates of glutamate in iCtrl and i*Xbp1* cells after 24h treatment with 10 mM NAC (n ≥ 3).

(O) Schematic illustration of the different intervention strategies used to interfere with GSH synthesis. (LPO = Lipid peroxidation).

(P) Fractional enrichment of serine M+3 in iCtrl and i*Xbp1* cells cultured in complete or serine/glycine-free (-S/G) medium supplemented with 17 mM [U-^{13}C] glucose tracer in the presence (+) and absence (−) of 15 mM BI-4916 for 24h (n = 3, two-Way ANOVA).

(Q) Intracellular serine level of iCtrl and i*Xbp1* cells after 24 h S/G starvation and co-treatment with 15 mM BI-4916 (n = 3).

(R) GSH level of iCtrl and i*Xbp1* cells; treated as in C (n ≥ 4).

(S) Relative percentage of FITC$^+$ cells in iCtrl and i*Xbp1* cells in complete or S/G-free medium and co-treatment with 15 mM BI-4916 (n ≥ 3).

(T) Relative cytoplasmic ROS level of iCtrl and i*Xbp1* cells after; treated as in C (n ≥ 2, paired t-test). *p < 0.05, **p < 0.01, ***p < 0.001.

To investigate whether the observed effects are generalizable to ER stress, we used the ER stress inducer Tunicamycin (TM) in iCtrl cells and were able to phenocopy the glutamate release phenotype of i*Xbp1* cells in a dose-dependent manner (Figure 1J). In line with this finding, we also observed increased cystine uptake rates upon TM treatment. Surprisingly, TM treatment triggers a switch from glycine release toward glycine uptake (Figures 1K and 1L). In contrast, serine consumption was not altered and only elevated at higher TM doses in i*Xbp1* cells (Figure 1M). Generally, serine catabolism provides sufficient amounts of glycine resulting in the net excretion of glycine.[37,38] However, in context of ER stress, serine-derived glycine seems not to be sufficient for IECs resulting in a switch from net excretion to net consumption. Similar results were also observed in intestinal organoids (Figures 1N and 1O). Interestingly, the obtained data suggest a higher baseline stress level in organoids compared to the 2D cell culture model.

Overall, our findings demonstrate that chronically ER-stressed IECs promote GSH synthesis by modulating the uptake of GSH-relevant amino acids from the extracellular space.

Metabolic reprogramming of the one-carbon metabolism fuels the NADPH pool upon endoplasmic reticulum stress

In addition to providing glycine for GSH synthesis, the 1C metabolism can directly supply NADPH thereby contributing to cellular RedOx balance.[39] Depending on the cellular demands, cells can convert 1C units via MTHFD1L into formate generating ATP or fully oxidise 1C units via ALDH1L1/L2 to CO_2 generating NADPH (Figures 2A and S2A).[18] Since previous studies indicate that ER stress increases intracellular ROS levels,[40,41] we postulated a metabolic rewiring toward ALDH1L1 or ALDH1L2 to enhance the reducing capacity in response to ER stress. Increased NADPH levels and unchanged formate release rates in i*Xbp1* cells indeed indicated that ER-stressed IECs favored the full oxidation of 1C units to CO_2 to generate NADPH (Figures 2B and 2C). As expected, i*Xbp1* cells showed increased *Aldh1l2* expression at gene and protein level compared to iCtrl cells. Stimulation with TM also triggers *Aldh1l2* upregulation (Figures 2D and S2B). ER stress-dependent induction of *Aldh1l2* was also confirmed in intestinal organoid (Figure 2E). Next, we analyzed the gene expression status of additional 1C genes and observed that ER-stressed IECs predominantly increase the expression of the mitochondrial 1C genes *Shmt2*, *Mthfd2* and *Aldh1l2* whereas the expression of its cytosolic counterparts including *Aldh1l1* was unaffected (Figure 2F).

Since the observed metabolic adaptations are crucial for maintaining cellular Redox homeostasis, we next checked the cytosolic ROS level. We noted increased ROS levels at baseline in i*Xbp1* cells which were further augmented in response to TM treatment (Figure 2G). In line with increased ROS levels, LPO was also significantly elevated in i*Xbp1* cells and further increased upon TM stimulation (Figure 2H). It was puzzling why the increase of GSH synthesis under chronic ER stress does not lead to sufficient intracellular neutralization of ROS and LPO species. Neutralization of ROS is conducted via the reduction of hydroperoxides by glutathione peroxidases (GPXs).[42] We therefore tested the expression of *Gpx1-4* and observed significantly reduced mRNA levels of all *Gpx* genes in *Xbp1*-deficient cells (Figure 2I). Probably, the reduced *Gpx* expression partially accounts for the increased accumulation of ROS in chronically ER-stressed cells. However, despite of increased Redox stress in *Xbp1* deficient cells, we did not observe any differences in proliferation, indicating that the metabolic adaptations prevent major oxidative damage (Figure 1J). To test if metabolic adaptations in i*Xbp1* cells are indeed the consequence of elevated ROS, we used ROS scavengers to rescue the metabolic phenotype (Figure 2K). Treatment with the antioxidant N-acetyl-cysteine (NAC) successfully lowered intracellular ROS and LPO levels (Figure 2L+M). Most strikingly, NAC treatment also reverted the observed glutamate switch in i*Xbp1* cells (Figure 2N). In sum, our findings illustrate that metabolic rewiring is directly linked to ER stress-mediated ROS increase.

To test the importance of the observed metabolic polarization in ER-stressed IECs, we targeted GSH homeostasis by limiting intracellular serine and glycine availability (Figure 2O). We therefore deprived iCtrl/iXbp1 cells of serine/glycine (S/G) to limit GSH precursor availability. A decrease of intracellular serine and glycine levels as well as an accumulation of the precursor γ-L-glutamyl-L-cysteine (GGC) confirmed the effectiveness of the S/G starvation (Figures S2C–S2E). However, under S/G deprivation, cells are able to activate the serine *de novo* synthesis pathway (SSP) to generate serine from glucose.[43] To test for this compensatory mechanism, we performed [U-^{13}C]-glucose tracing to monitor the relative glucose flux through the SSP. Illustrated by the M+3 serine isotopologue, S/G starvation strongly increased the flux through SSP. Of note, at standard conditions, the SSP activity of iXbp1 cells was not increased compared to iCtrl cells (Figure 2P). As the compensatory activation of SSP might directly feed into GSH synthesis, we combined S/G starvation with PHGDH inhibition, the rate limiting enzyme of the SSP pathway, by using the competitive inhibitor BI-4916.[44,45] As expected, BI-4916 treatment blocked SSP activity, and dual perturbation with BI-4916 and S/G starvation further reduced intracellular serine and GSH levels, confirming the efficacy of our treatment (Figures 2P–2R). Interestingly, GSH depletion was more pronounced in iXbp1 cells compared to iCtrl cells (Figure 2R).

To assess whether the metabolic shift toward reduced GSH levels functionally mimicked the RedOx imbalance phenotype observed upon chronic ER stress, we measured ROS and LPO levels in the presence of different interventions. Indeed, S/G deprivation with or without SSP inhibition led to increased LPO and ROS accumulation, which was again more pronounced in iXbp1 cells. In contrast to S/G deprivation, sole inhibition of SSP neither increased ROS nor diminished GSH level (Figures 2R and 2T), indicating that the extracellular supply with S/G is the major source for GSH precursors and compensates for SSP loss in IECs. Although the cause for the impaired Redox homeostasis is slightly different, both chronic ER stress as well as GSH limitation led to an inefficient removal of ROS and LPO species in IECs. Thus, our data point out that S/G supply is important to ensure proper RedOx homeostasis in ER-stressed IECs.

Overall, our data indicate that ER stress induces a metabolic shift toward GSH metabolism to counterbalance ROS. Furthermore, we identify a distinct reprogramming of the 1C metabolism in response to ER stress to ensure sufficient NADPH supply. Both metabolic adaptations are essentially needed to ensure a healthy Redox balance to sustain the proliferation of IECs.

Metabolic rewiring toward glutathione and NADPH synthesis is of physiological relevance in patients with inflammatory bowel diseases

To validate whether the metabolic adaptation of serine, glycine, and 1C (SGOC) metabolism contributes to the pathogenesis of IBD, we analyzed transcriptome dataset from patients with UC and CD.[46] Despite the low patient quantity, we observed a significant increase of *SLC7A11* and *ALDH1L2* expression in inflamed sigmoid colon biopsies of patients with UC, and a similar trend in patients with CD. In contrast, no expression changes were observed in non-inflamed UC patient as well as in samples from the healthy and disease control group (Figure 3A).

To validate these results, we analyzed two different transcriptome datasets from large UC patient cohorts.[47,48] We first tested the hypothesis that ER stress might contribute to the metabolic adaptations in the inflamed mucosa of patients with UC. We therefore analyzed the relation of mucosal ER stress with the degree of inflammation by correlating disease severity with a previously published colon-specific ER stress signature.[14] We discovered a significant correlation of ER stress and endoscopic and histologic disease severity (Figures 3B and S3A). Additionally, we observed a strong correlation of ER stress and an ISG signature[32] pointing toward a direct link between ER stress and mucosal inflammation (Figures 3C and S3B). We further delineated that the SSP including *PHGDH*, *PSAT1*, and *PSPH* (SSP score) strongly correlated with disease severity (Figures 3D and S3C) as well as the amplitude of ER stress (Figures 3E and S3D). Moreover, we also validated our *in vitro* findings and observed an increase in *SLC7A11* as well as a decrease in *GPX4* expression which was coupled to both parameters (Figures 3D, 3E, S3C, and S3D). Remarkably, the mitochondrial 1C gene score (Mito 1C, scoring *SHMT2*, *MTHFD2*, and *ALDH1L2*) was also strongly linked to both parameters. In contrast, the cytosolic 1C genes score (Cyto 1C, scoring *SHMT1*, *MTHFD1*, and *ALDH1L1*) did not show any dependency. By considering the gene expression ratios of the mitochondrial 1C enzymes over their cytosolic counterparts, we further support our *in vitro* findings in ER-stressed IECs. We observed a disease severity-dependent activation of the mitochondrial 1C metabolism in both transcriptome datasets (Figures 3F and S3E). Additionally, colon biopsies of patients with UC also showed an increased expression of the mitochondrial 1C enzymes compared to healthy controls (Figure S3F).[49] Next, we checked the expression status of genes related to the SGOC metabolism in *Xbp1*-deficient mice as a model to mimic chronic ER stress in the gut.[7,50] Due to the limited sample number, we did not detect significant differences. However, we observed similar changes in regard to the upregulation of mitochondrial 1C and SSP (Figures S3G and S3H).

To further substantiate the hypothesis that the metabolic rewiring corresponds with disease activity in IBD, we assessed the differential changes of Mito1C and SPP signatures in patients with UC under biologic therapy. Interestingly, the targeted treatment with biologic therapies led to a significant reduction of the metabolic signature in therapy-responding patients, suggesting that the metabolic remodeling is an important protective cellular adaptation to counterbalance chronic inflammation (Figure 3G).

As our data collectively demonstrate that a metabolic rewiring of the SGOC metabolism takes place in patients with IBD, we furthermore aimed to understand whether this is a cell type-specific adaptation to ER stress. We therefore evaluated single-cell RNA sequencing (scRNA-Seq) data obtained from the SCP259 scRNA-Seq IBD dataset (colon mucosa of 18 patients with UC and 12 healthy individuals[51]). We observed in different epithelial cell clusters an upregulation of SSP and mitochondrial 1C genes in a disease activity-dependent manner, which correlates with the amplitude of the ER stress signature (Figures S3I and S3J). Interestingly, this metabolic adaptation was predominantly found in clusters of secretory epithelial cells (secretory TA, immature goblet cells) and transient amplifying (TA) cells, stem cells, which are, due to their proliferative and secretory demand, highly dependent on effective endoplasmic reticulum function. In summary, transcriptome data from patients with UC further corroborate a crucial role of metabolic reprogramming of 1C metabolism in the context of intestinal inflammation.
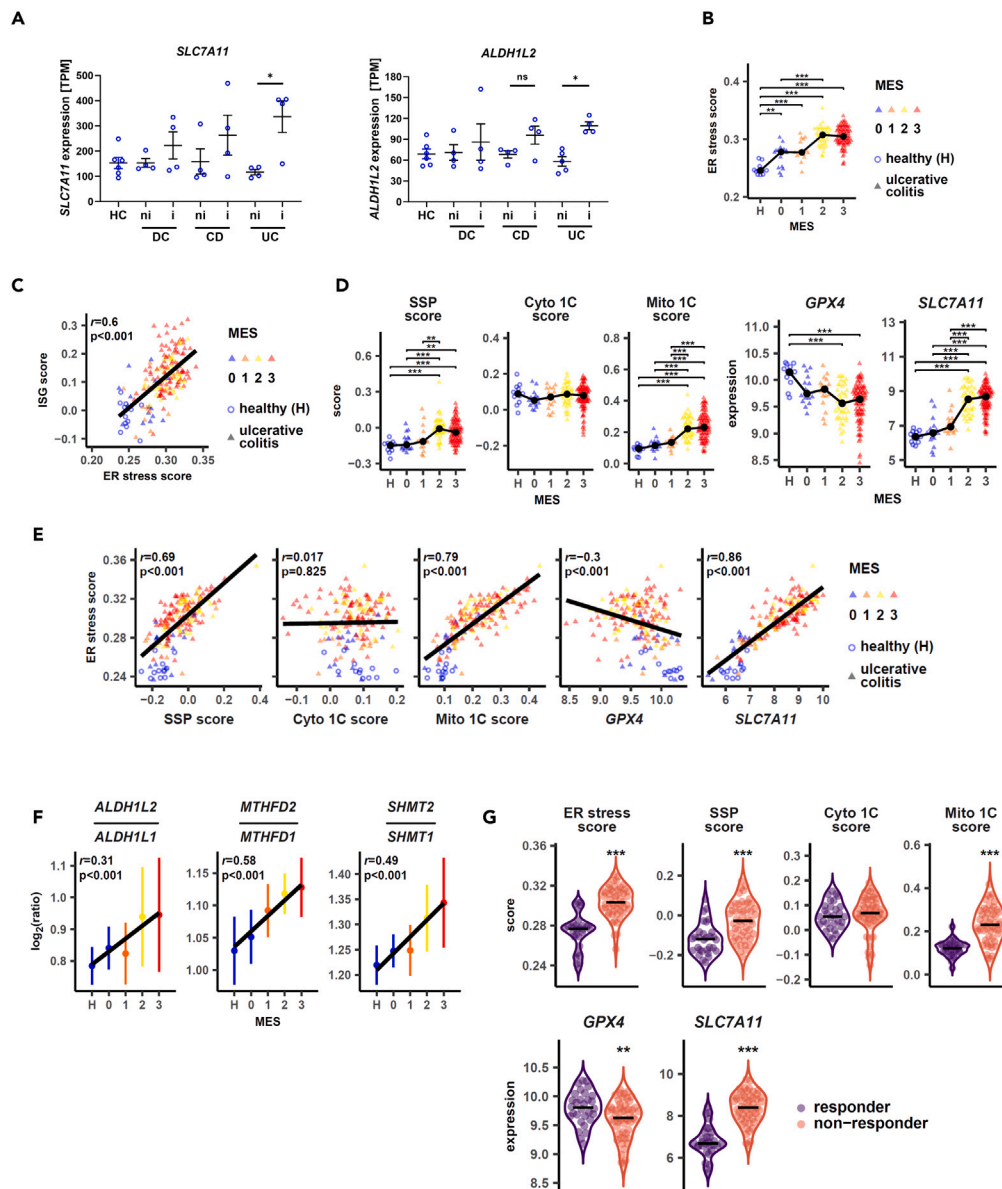
Figure 3. Metabolic adaption of the serine metabolism occurs in the inflamed intestinal epithelium of patients with IBD

(A) RNAseq data analysis of *SLC7A11 and ALDH1L2* in patient samples derived from the sigmoid colon region. Samples derived from healthy donor (HC) or non-inflamed (ni) and inflamed (i) areas of patients with Crohn's (CD) or patients with ulcerative colitis (UC). Inflamed and non-inflamed samples from an inflammatory disease unrelated to IBD serve as disease control (DC) (n ≥ 4 patients).

(B) Correlation of ER stress with endoscopic MAYO score (MES) in patients with UC using the GSE73661 dataset and the singscore calculation method. ER stress signature is defined by Powell et al. and includes 62 genes enriched in the colonic epithelial cells upon ER stress.[14] Black dots and connecting lines show the median expression.

(C) Correlation of ER stress with the interferon-stimulating gene signature[32] in the GSE73661 dataset. Pearson's correlation coefficients *r* and p values are shown.

(D) SGOC metabolism related gene expressions and scores according to MES in patients with UC from the GSE73661 dataset. Black dots and connecting lines show the median expression.

(E) Correlation of SGOC metabolism-related gene expression with ER stress and disease severity in the GSE73661 dataset. Pearson's correlation coefficients *r* and p values are shown.

(F) Gene expression ratios of the mitochondrial 1C cycle enzymes over their cytosolic counterparts (*ALDH1L2/ALDH1L1, SHMT2/SHMT1, MTHFD2/MTHFD1* and their correlation with IBD severity.

(G) Correlation of ER stress and the expression of SGOC metabolism-related genes in patients from the dataset GSE73661 according to therapy response status
*p < 0.05, **p < 0.01, ***p < 0.001.
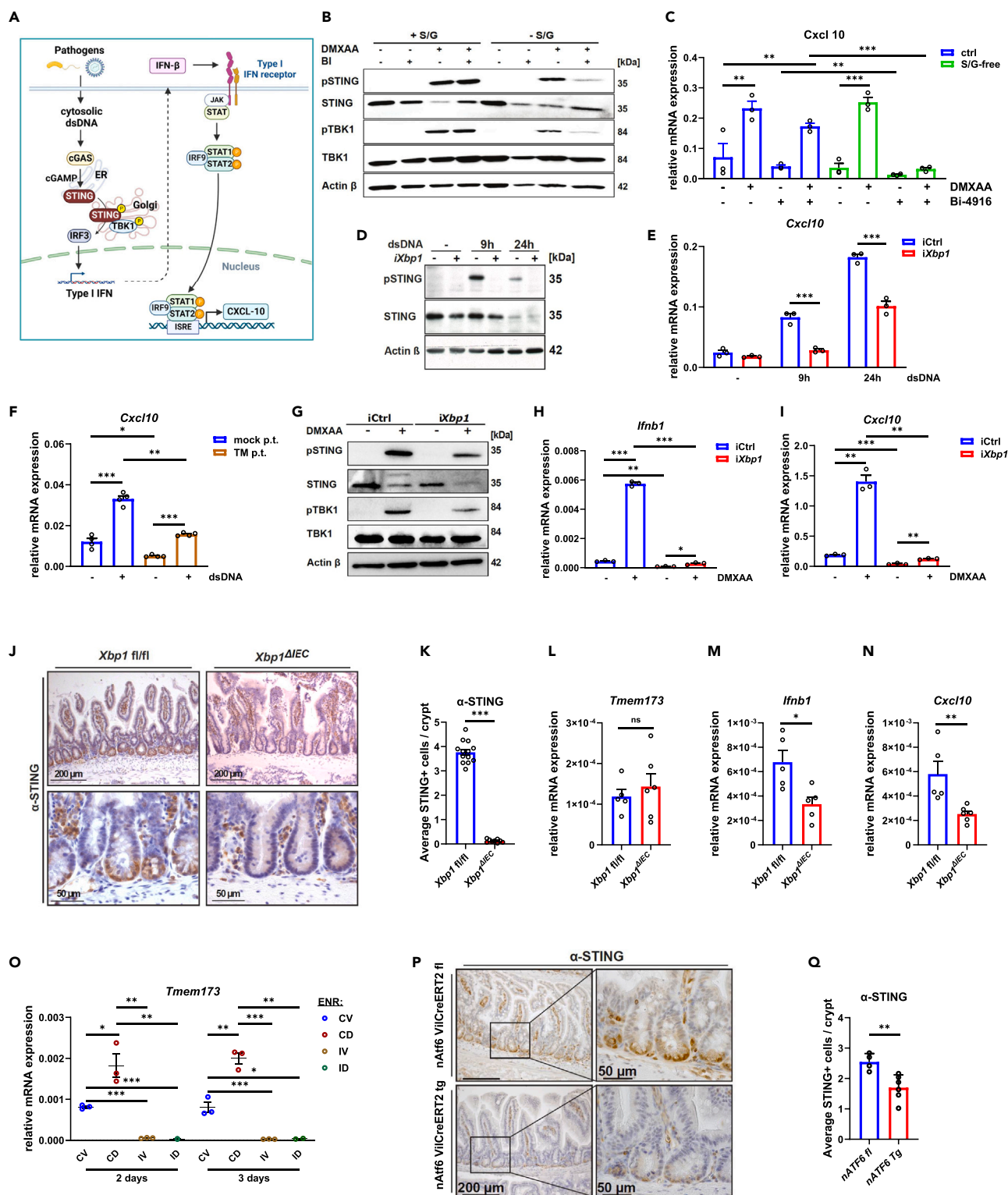
Figure 4. Chronic ER stress-induced RedOx imbalance dampens cGAS-STING signaling *in vitro* and *in vivo*

(A) Schematic outline of the cGAS-STING signaling and its downstream targets.

(B) Western Blot analysis of iCtrl cells stimulated with DMXAA (100 μg/mL, 1h) after cultivation in complete or S/G-free medium for 24h and co-treatment with 15 mM BI-4916.

Figure 4. Continued

(C) *Cxcl10* gene expression of iCtrl and i*Xbp1* cells which were starved for S/G and treated with 15 μM BI-4916 for 24h before stimulation with DMXAA (100 μg/mL, 3h) (n = 3).

(D) Western Blot analysis of STING activation in iCtrl and i*Xbp1* cells stimulated with dsDNA (1 μg/mL) for the indicated time points.

(E) *Cxcl10* gene expression of the experiment shown in (D) (n = 3).

(F) *Cxcl10* gene expression in dsRNA-stimulated (1 μg/mL) iCtrl cells pretreated with or without 0.1 μg/mL Tunicamycin (n = 4).

(G) iCtrl and i*Xbp1* cells were stimulated with DMXAA (100 μg/mL, 1h) and expression of the indicated proteins was assessed by Western blot.

(H and I) *Ifnb1* (H) and *Cxcl10* (I) gene expression of iCtrl and i*Xbp1* cells stimulated with DMXAA (100 μg/mL, 3h, n = 3).

(J) IHC staining of STING expression in *Xbp1*$^{fl/fl}$ (n = 13) and *Xbp1*^{ΔIEC} (n = 10) mouse supplemental information sections. Representative images.

(K) Corresponding quantification of STING-positive cells per crypt.

(L–N) *Tmem173* (L), *Ifnb1* (M), and *Cxcl10* (N) gene expression from SI crypts isolated from *Xbp1*$^{fl/fl}$ (n = 5) and *Xbp1*^{ΔIEC} (n = 6) mice.

(O) *Tmem173* gene expression in murine SI organoid cultures enriched for stem cells (CV), Paneth cells (CD), enterocytes (IV), and Goblet cells (ID) after cultivation in specific enrichment media (ENR) for 2days or 3days

(P) IHC staining of STING expression in *nATF6* VilCreERT2 tg or fl mice. Intestinal epithelial-specific overexpression of ATF6 was induced with Tamoxifen for 7days and sacrificed after another 4days. Representative HE/STING-stained supplemental information sections.

(Q) Corresponding quantification of STING-positive cells per crypt (n = 4 (fL) and n = 6 (tg)).*p < 0.05, **p < 0.01, ***p < 0.001.

Chronic endoplasmic reticulum stress-induced reduction/oxidation imbalance leads to cGAS-STING signaling exhaustion

Having established the importance of 1C metabolism in the intestinal epithelium, we wondered whether ER stress induced alterations in the 1C metabolism affect innate immune pathways relevant for IBD. It is widely accepted that the disease extent and disease severity of patients with IBD directly correlate with an increased risk of viral infection such as CMV,[3,52] representing a major clinical challenge in the disease management. As CMV control critically depends on cGAS-STING dependent IFN-production,[53] and both ROS and by-products of the LPO reactions (e.g., 4-HNE) suppress cGAS-STING signaling by either preventing STING dimerization or its transition from the ER to the Golgi compartment (Figure 4A),[23,54] we tested a potential crosstalk between the observed ER stress-induced metabolic imbalance and cGAS-STING signaling in IECs.

Since our previous experiments indicate that S/G deficiency as well as chronic ER stress cause an accumulation of ROS and LPO species, we asked whether S/G deprivation disrupts epithelial STING signaling. We limited S/G availability by either the single (S/G starvation) or double intervention (S/G starvation + PHGDHi) and analyzed STING activation in iCtrl cells in the presence or absence of the STING agonist DMXAA. While S/G starvation or BI-4916 treatment alone had no significant impact on STING activation, dual perturbation resulted in the decreased phosphorylation of STING and its downstream target TBK1 (Figure 4B). Additionally, a strong and significant reduction of *Cxcl10* expression was observed following the dual treatment (Figure 4C). Altogether, our data show that the supply of serine and glycine is critical to facilitate proper STING/IFN-I signaling in ER-stressed IECs.

As *Xbp1* deficiency also induces RedOx imbalance in a GSH-dependent manner, we postulated that chronic ER stress impairs the IFN response to viral infection. To test this hypothesis, we stimulated iCtrl and i*Xbp1* cells with double-stranded (ds) DNA and noticed a strong abrogation of STING activity (Figure 4D) and *Cxcl10* expression (Figure 4E) in *Xbp1*-deficient IECs. This observation was phenocopied by treating wild-type cells with the chemical ER stress inducer TM prior to dsDNA exposure (Figure 4F). Our findings suggest that unresolved ER stress promoted the exhaustion of the STING pathway with impaired IFN-I and CXCL10 production in response to pathogen sensing. Indeed, the STING agonist DMXAA activated STING and TBK1 phosphorylation in iCtrl cells whereas the effect was reduced in i*Xbp1* cells (Figure 4G). This finding was accompanied by impaired *Ifnb1* and *Cxcl10* induction (Figures 4H and 4I). Collectively, our data support the hypothesis that the metabolic reprogramming of the 1C metabolism upon ER stress directs STING signaling in the intestinal epithelium.

Next, we aimed to understand the *in vivo* consequences of chronic ER stress on cGAS-STING signaling. We thereby took advantage of an intestinal-specific conditional *Xbp1* knockout mouse model and analyzed STING expression as well as IFN-I-activity.[7,55] We noted that *Xbp1*^{ΔIEC} mice showed significantly reduced STING expression compared to *Xbp1*$^{fl/fl}$ (wild type) littermates (Figure 4J). Especially the crypt-specific STING expression was strongly abolished upon the deletion of *Xbp1* (Figures 4K and S4A). Notably, reduced STING protein expression was unrelated to *Sting* transcription (Figure 4L), indicating post-translational regulation. Additionally, we observed reduced *Cxcl10* and *Ifnb1* expression in small intestinal (SI) crypts from *Xbp1*^{ΔIEC} mice, an indication for abrogated STING/IFN-I activity (Figures 4M and 4N). Lastly, we co-validated the impact of prolonged ER stress on epithelial cGAS-STING signaling using an independent transgenic mouse model, i.e., *nAtf6*^{IEC} VilCreERT2 mice carrying a Tamoxifen-inducible intestinal epithelial *Atf6* overexpression (leading to constitutive ER stress[56,57]). Tamoxifen-induced overexpression of *Atf6* also evoked epithelial STING suppression (Figures 4P and 4Q).

To reveal which specific cell-type predominantly expresses STING in the intestinal epithelium, we subjected SI organoids to different conditioned media to enrich for specific epithelial lineages, i.e., stem cells, Paneth cells, Goblet cells, and enterocytes (Figure 4O).[58] Lysozyme expression confirmed the SI organoid differentiation into the different epithelial lineages (Figures S4B and S4C). Notably, *Tmem173* expression was most pronounced in Paneth cell-enriched organoids (ENR-CD) and stem cell-enriched organoids (ENR-CV), while enrichment for enterocytes (ENR-IV) or goblet cells (ENR-ID) did not show *Tmem173* expression (Figure 4O). The finding that Paneth cells predominantly express STING and that *Xbp1* loss is known to trigger increased Paneth cell death in intestinal crypts[7] further corroborates a crucial connection between ER stress and mitochondrial 1C metabolism on cGAS-STING signaling.
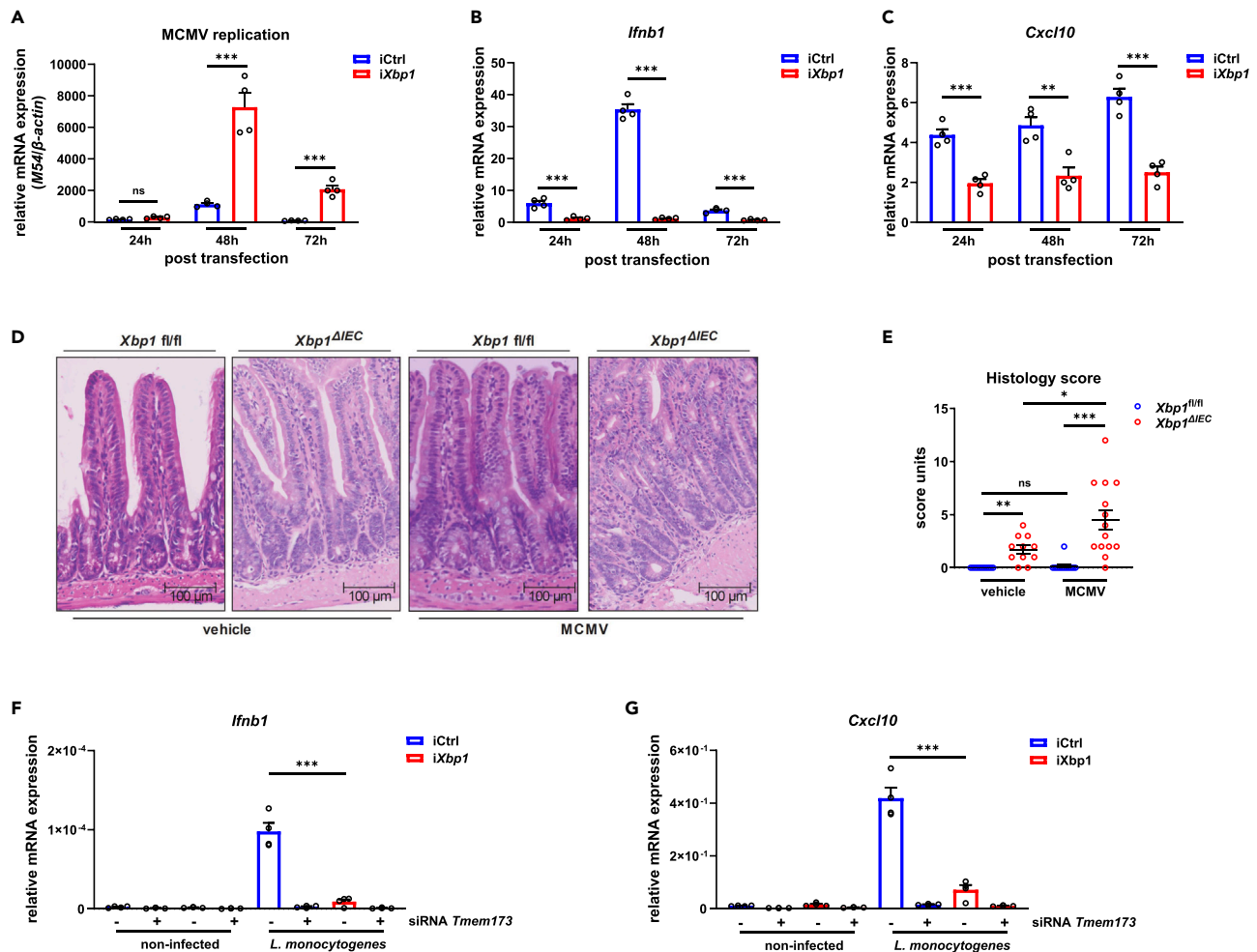
Figure 5. Chronic ER stress increases susceptibility to bacterial and viral infections

(A–C) iCtrl and i*Xbp1* cells were infected with MCMV at a MOI of 10 and MCMC viral load (A), *Ifnb1* (B), and *Cxcl10* (C) gene expression was assessed by qRT-PCR (n = 4).

(D and E) *Xbp1*^fl/fl and *Xbp1*^ΔIEC mice were infected intraperitoneally with vehicle (n = 11 for each group) or MCMV (n = 12 (*Xbp1* fl/fl); n = 14 (*Xbp1*^ΔIEC)) and intestinal inflammation was assessed via histology. Representative images of HE stained supplemental information sections (D) and quantification of the histology score (E) are illustrated.

(F and G) iCtrl or i*Xbp1* cells in the presence (+) or absence (−) of *Tmem173* were exposed to *Listeria monocytogenes* at a MOI of 50 for 1h before medium was exchanged and Gentamicin (50 μg/mL) was added for 1h, followed by Gentamicin at 5 μg/mL for 22 h. STING activation was monitored via the *Ifnb1* (F) and *Cxcl10* (G) gene expression (n = 4). *p < 0.05, **p < 0.01, ***p < 0.001.

Chronic endoplasmic reticulum stress increases susceptibility to bacterial and viral infections

To test whether ER stress-induced perturbation of STING signaling links to susceptibility to viral or bacterial infections, we infected i*Xbp1* cells (and controls) with murine CMV (MCMV) and assessed STING-dependent IFN-I production. Indeed, iCtrl cells responded to MCMV infection with STING activation, IFN-I induction, and subsequent viral containment (Figures 5A–5C). In contrast, *Xbp1*-deficient cells showed an increased MCMV load and failed to induce *Ifnb1* and *Cxcl10* expression. To verify the impact of epithelial STING signaling on CMV infection *in vivo*, we challenged *Xbp1*^fl/fl and *Xbp1*^ΔIEC mice with MCMV intraperitoneally. Five days after the initial infection, we measured the degree of intestinal inflammation, as described previously.[59,60] In line with previous reports, the total viral load within the intestinal mucosa was not detectable on the day of sacrifice. However, we observed increased severity of enteritis by a semi-quantitative histology score in *Xbp1*^ΔIEC, but not in *Xbp1*^fl/fl mice (Figures 5D and 5E). This observation confirmed that MCMV infection controlled the inflammatory tone in genetically susceptible mice that exhibit chronic epithelial ER stress. Finally, we infected IECs with the intracellular pathogen *Listeria monocytogenes* to test whether the observed STING exhaustion is also relevant to bacterial infection. As described before,[61] *L. monocytogenes* infection resulted in strong *Cxcl10* and *Ifnb1* induction in iCtrl cells, which was barely detectable in i*Xbp1* cells (Figures 5F and 5G).

Collectively, our data indicate that ER stress causes a functional impairment of STING signaling which leads to inefficient pathogen clearance in the intestinal epithelium.
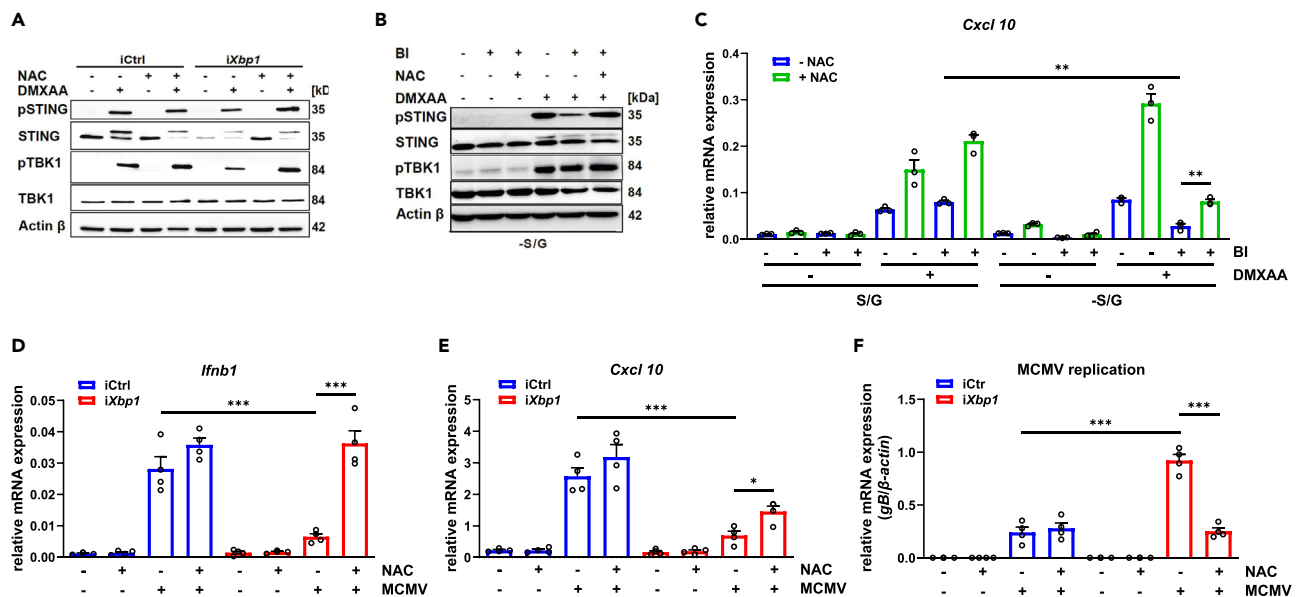
Figure 6. Antioxidant therapy restores cGAS-STING signaling and improves CMV infection control in intestinal epithelial cells

(A) Western Blot analysis of iCtrl and i*Xbp1* cells stimulated with DMXAA (100 μg/mL, 1h) after 24h pretreatment with 10 mM NAC.

(B) Western blot analysis of iCtrl cells stimulated with DMXAA (100 μg/mL, 1h) after cultivation in complete or S/G-free medium for 24h in the presence or absence of 10 mM NAC and 15 mM BI-4916.

(C) *Cxcl10* gene expression of iCtrl stimulated with DMXAA (100 μg/mL, 3h) after 24 h S/G starvation and co-treatment with 10 mM NAC and 15 mM BI-4916 (n = 3).

(D–F) iCtrl and i*Xbp1* cells were stimulated with 10 mM NAC and infected with MCMV (MOI = 1). mRNA expression of *Ifnb1* (H), *Cxcl10* (I) as well as viral load (J) (measured by viral DNA copy number) were determined via qRT-PCR (n = 4). *p < 0.05, **p < 0.01, ***p < 0.001.

Antioxidant therapy restores cGAS-STING signaling and cytomegalovirus control in intestinal epithelial cells

After demonstrating that antioxidant treatment alleviates the ER stress-mediated metabolic adaptation in IECs, we finally tested the hypothesis that NAC supplementation restores epithelial STING signaling and thus protects against CMV infections. We observed that antioxidant treatment restored DMXAA-induced STING and TBK1 phosphorylation in i*Xbp1* cells (Figure 6A), showing that ER stress indeed impairs STING signaling via ROS and/or LPO generation. Alternatively, GPX4 inhibition, using the GPX4 inhibitor RSL3, led to a nearly complete abrogation of STING signaling in iCrtl cells, which was rescued by NAC treatment (Figures S5A and S5B). Similarly, the impact of combined S/G starvation and PHGDH inhibition on STING signaling was partially neutralized in the presence of NAC (Figures 6B and 6C). Finally, we wondered whether the restoration of STING signaling via NAC treatment directly improves CMV infection control in IECs. To this end, we co-treated MCMV infected iCtrl and i*Xbp1* cells with the antioxidant. In line with our hypothesis, i*Xbp1* cells showed a robust restoration of IFN-I signaling (Figures 6D and 6E) which further resulted in the reconstituted suppression of the MCMV viral load (Figure 6F). Collectively, our data suggest that ER stress-derived ROS increase limits STING signaling, representing the underlying reason for impaired viral control.

DISCUSSION

The intestinal epithelium is not only critical for nutrient and water absorption from food but also forms a tremendous protective barrier against the outer environment.[62] Due to the frequent exposure to extrinsic and intrinsic stress stimuli (e.g., nutrient availability, harmful pathogens, microbiota-derived metabolites and so forth), cells have to constantly adapt their cellular and metabolic programs to maintain intracellular homeostasis.[63] Although prior studies already showed a direct link between the manifestation of chronic ER stress and the development of IBD,[33,64] there is a limited understanding of how IECs fine-tune their metabolism to deal with unresolved ER stress and related gut inflammation.

Here we demonstrate that chronically ER-stressed IECs activate a distinct metabolic program to boost GSH synthesis. We thereby observed that IECs actively increase the intracellular availability of amino acids especially required for GSH synthesis by modulating amino acid transporter activity in the plasma membrane. For example, upregulating of the SLC7A11 transporter system or increased glutamine uptake in response to chronic ER stress are two options for how IECs cover their additional cysteine and glutamate demands for GSH synthesis. Interestingly, the observed glycine switch is supported by data from human IECs. Howard et al. demonstrated that the glycine transporter SLC6A9 (Glyt1) is crucial to maintain intracellular GSH level upon increased oxidative stress.[65] Previous data indeed indicate that the fine-tuning of amino acid transporters including SLC6A9 and SLC7A11 is one common strategy to cover the specific amino acid demands upon ER stress.[66] Surprisingly, depending on the ER stress amplitude, IECs seems to coordinate the support of GSH synthesis differently. Under chronic ER stress, IECs utilize serine as the main source to cover cellular glycine demands. In contrast, the direct uptake of extracellular glycine

is favored upon acute ER stress conditions. In this case, the additional glycine demand for GSH synthesis most likely exceeds the maximal capacity of the SSP to provide precursors for both GSH and purine synthesis.[67] Interestingly, the dependency on extracellular glycine is presumably compensated by the long-term metabolic and cellular adaptations in chronically ER-stressed IECs.

We further showed that IECs induce a second compensatory mechanism by upregulating the mitochondrial arm of the 1C cycle toward ALDH1L2. Thus, IECs are an excellent showcase for the proposed metabolic flexibility of the 1C metabolism and shows how ER-stressed cells maximize their supply for GSH synthesis under ER stress conditions.[18] Firstly, the SHMT2 reaction provides additional glycine as a building block for GSH. Secondly, ALDH1L2 upregulation increases NADPH supply. Since the mitochondrial and cytosolic NADPH pools are separated from each other and NADPH shuttling does not occur,[68] the additional NADPH presumably boosts the conversion of mitochondrial GSSG to GSH. Several studies already showed that ALDH1L2 is of great importance to regulate mitochondrial ROS level.[69–72] However, we cannot exclude that other metabolic sinks for ALDH1L2-derived NADPH exist in ER-stressed IECs. For example, under normal growth conditions, ALDH1L2-derived NADPH is known to support proline biosynthesis.[72]

Although the mechanistic basis for the metabolic reprogramming in IECs deserves to be resolved in more detail, recent studies suggest a critical role for the PERK-ATF4-pathway and the integrated stress response (ISR).[73–75] CHIPseq data already demonstrated that *PHGDH*, *PSAT1*, *SHMT2*, *MTHFD2*, and *ALDH1L2* are direct ATF4 targets.[76] Additionally, several amino acid transporters including *SLC7A11* and *SLC6A9* and the serine transporters *SLC1A4* as well as *SLC1A5* possess ATF4 binding sites and are upregulated in response to ER stress in a PERK-dependent manner.[66,76] Along the same line, both deletion of ATF4 or ISR inhibition prevent the transcriptional upregulation of *ALDH1L2*, *SLC7A11*, and *SLC6A9* in FH- and SDH-deficient cells.[75] Interestingly, recent data demonstrate that glucose limitation also causes an upregulation of the mitochondrial 1C cycle toward *ALDH1L2*, whereas the underlying mechanism(s) are not completely explored and might also be related to increased ER stress.[39,77]

Paradoxically, although both metabolic adaptations are designed to increase the antioxidant capacity of IECs, chronic ER stress causes a state of RedOx imbalance. Based on our findings, we postulate that IECs remodel their amino acid and 1C metabolism to accelerate the detoxification of ROS species upon ER stress. Due to this metabolic adaptation, IECs normally receive a short-term buffer to activate compensatory mechanism(s) (e.g., UPR activation, increase of ER folding capacity and so forth) and to restore cellular homeostasis. If ER stress is not resolved in this initial phase or malfunctions of the compensatory systems (e.g., UPR) occurs, the rising ROS burden overwhelms the cellular detoxification systems and disrupts the RedOx balance. Despite of increased ROS, the metabolic reprogramming is still sufficient to guarantee the survival of Xbp1-deficient IECs indicated by their capability to maintain growth rates similar to those of wild-type cells. Since prolonged ER stress is known to inhibit global protein translation,[78] it is not surprising that several GPXs are less expressed, giving a possible explanation why Xbp1-deficient IECs fail to completely restore RedOx homeostasis in the long run. Interestingly, the GSH-dependent GPX GPX4 is essential for the conversion of harmful lipid hydroperoxides into non-toxic lipid alcohols,[79] partially explaining the increased LPO level observed in our chronic ER stress model. Intriguingly, S/G starvation also leads to an increase in ROS and LPO. In contrast to the reduced GPXs activity upon chronic ER stress, GSH limitation is the driving force for a deregulated RedOx balance upon S/G deprivation. Both chronic ER stress as well as S/G starvation increase the GSH dependence of IECs and links our metabolic phenotype to GSH metabolism. Notably, our rescue experiments with the antioxidant NAC further underpin our notion that the metabolic rewiring represents a compensatory response to ER stress and is coupled to an increase in ROS.

Importantly, our computational analysis demonstrates the *in vivo* relevance of the metabolic compensatory program in a clinically relevant disease context. We directly linked the metabolic phenotype to the amplitude of ER stress, the degree of inflammation as well as the disease severity status of patients with UC. Beside the activation of the mitochondrial 1C cycle and SSP (also shown in Xbp1-deficient mice), patients with UC also showed *SLC7A11* upregulation and *GPX4* downregulation in an ER stress-dependent manner. Interestingly, increased LPO levels and reduced GPX4 activity are already reported in CD,[80] supporting our notion that our findings are also relevant for patients with CD. Our single cell analysis further reveal a cell-type specificity. Especially TA stem and immature goblet cells show the metabolic adaptation, whereas other cell types (e.g., enterocytes, M cells) presumably rely on SGOC-independent mechanisms to cope with increased ER stress. Another interesting observation in TA cells is that increased mitochondrial activity is accompanied with reduced cytosolic 1C activity. Previous studies already reported that UPR defects induce a hyper-proliferative IEC phenotype in mice[7] and that UPR activation is described as an important mediator for the transition of stem cells into TA cells.[81] Therefore, it would be interesting to check whether the metabolic rewiring of the SGOC is not only crucial for RedOx control but might also represent an important gatekeeper to maintain a healthy epithelial lining and to prevent uncontrolled crypt growth. From the clinical point of view, the fact that the metabolic signature is strongly linked to both disease severity and therapy-response could be exploited to define the severity grade and/or therapy-response status of patients with UC in the future.

Our finding that the ER stress-mediated impairment of the cGAS-STING signaling increases the susceptibility toward CMV infection is of great clinical importance. Mucosal CMV infections are a leading cause of complicated disease course in IBD.[82,83] Up to now, the underlying molecular pathophysiology driving increased susceptibility toward CMV colitis in patients with IBD are poorly understood. In this study, our data provide a novel molecular nexus on how chronic ER stress paves the susceptibility to CMV infection and thereby generate a molecular inside into a well-established and highly relevant disease complication in IBD. We thereby found first evidences that chronic ER stress-caused RedOx imbalance prevents an efficient ROS/LPO clearance which inhibits cGAS-STING signaling. Our hypothesis is further underpined by our antioxidant rescue results, which are in line with other studies demonstrating that both ROS and LPO by-products are able to disrupt STING function.[23,54] However, our *in vivo* results related to Paneth cells suggest that additional cell-type specific consequences of ER stress might contribute to the overall impaired intestinal cGAS-STING-response. With regard to our antioxidant experiments, several studies demonstrated that ROS inhibition suppresses viral replication. Multiple herpesviruses are able to promote intracellular ROS generation and thereby

support their own replication.[84] In this context, it is shown that NAC supplementation inhibits the lytic replication cycle of Kaposi's sarcoma-associated herpesvirus *in vivo*.[85] Additionally, MHC68 replication is also suppressed in NAC-treated mice in an STING-dependent manner,[54] pointing toward a direct link between ER stress-induced ROS increase, impaired cGAS-STING signaling and viral replication. We therefore postulate that the metabolic reprogramming has a profound impact on host immunity and might provide a layer of susceptibility toward pathogen infection in the inflamed mucosa of patients with IBD. Recent data indeed indicate that the intestinal epithelium represents the primary sensor of mucosal CMV infection (46). Overall, our data strongly put forward the idea of an ER stress-driven immune exhaustion of the cGAS-STING pathway in the intestinal epithelium as a critical layer of susceptibility for CMV infection in IBD. Thus, our findings might pave the way toward future healthcare concepts to increase the viral control in patients with IBD.

Limitations of study

While our S/G starvation experiments provide evidence that IECs remodel their GSH metabolism in response to ER stress to sustain cGAS-STING signaling, we did not exhaustively test the impact of the mitochondrial 1C cycle (especially ALDH1L2) on this viral defense pathway. Additionally, we showed that our findings regarding the metabolic phenotype were also relevant in the context of IBD. However, we exclusively focused on patients with UC cohorts, even though patients with CD show signs for a comparable metabolic remodeling toward GSH and 1C metabolism. Although we demonstrate that chronic ER stress impairs STING signaling and CMV control in different murine models, our *in vivo* work is limited. In the future, it would be desirable to investigate the *in vivo* consequences of SG limitation on cGAS-STING signaling in murine models in more detail. In this study, our infection models were solely based on murine CMV due to species-specific replication restrictions.[86] Thus, the direct translation of all our findings to human CMV may be difficult without further investigation. Since direct *in vivo* experiments with human CMV are difficult, the usage of humanized mouse models could represent an alternative strategy to confirm our main findings in the future.[87]

STAR★METHODS

Detailed methods are provided in the online version of this paper and include the following:

- KEY RESOURCES TABLE
- RESOURCE AVAILABILITY
  - Lead contact
  - Materials availability
  - Data and code availability
- EXPERIMENTAL MODEL AND STUDY PARTICIPANT DETAILS
  - Mice
  - Cell lines
  - Organoid generation
- METHOD DETAILS
  - Chemicals and siRNA-mediated knockdown
  - Cell culture
  - *In vivo* MCMV infection
  - *In vitro* MCMV infection and quantification of replication
  - Histology
  - Histology score CMV colitis
  - *Listeria monocytogenes* infection
  - STING immunohistochemistry and quantification
  - Cell growth analysis
  - Determination of NADPH level
  - Determination of GSH/GSSG ratio
  - Bioinformatic analysis of RNAseq and scRNAseq datasets
  - Stable isotope tracing and metabolite extraction
  - GC-MS-based determination of MIDs of intracellular metabolites
  - Analysis of medium exchange rates
  - Formate release rates
  - LC-MS measurements
  - YSI measurements
  - Flow cytometric analysis of LPO levels
  - Flow cytometric analysis of cytoplasmic ROS levels
  - Western blot analysis
  - Quantitative real-time PCR (qRT-PCR) analysis
- QUANTIFICATION AND STATISTICAL ANALYSIS

REFERENCES

1. Kaplan, G.G. (2015). The global burden of IBD: from 2015 to 2025. Nat. Rev. Gastroenterol. Hepatol. *12*, 720–727. https://doi.org/10.1038/nrgastro.2015.150.

2. Schenk, W., Klugmann, T., Borkenhagen, A., Klecker, C., Dietel, P., Kirschner, R., Schneider, E., Bruns, T., Stallmach, A., and Teich, N. (2019). The detection of the cytomegalovirus DNA in the colonic mucosa of patients with ulcerative colitis is associated with increased long-term risk of proctocolectomy: results from an outpatient IBD clinic. Int. J. Colorectal Dis. *34*, 393–400. https://doi.org/10.1007/s00384-018-3210-8.

3. Qin, Y., Wang, G., Kong, D., Li, G., Wang, H., Qin, H., and Wang, H. (2021). Risk Factors of Cytomegalovirus Reactivation in Ulcerative Colitis Patients: A Meta-Analysis. Diagnostics *11*, 1952. https://doi.org/10.3390/diagnostics11111952.

4. Grootjans, J., Kaser, A., Kaufman, R.J., and Blumberg, R.S. (2016). The unfolded protein response in immunity and inflammation. Nat. Rev. Immunol. *16*, 469–484. https://doi.org/10.1038/nri.2016.62.

5. Adolph, T.E., Tomczak, M.F., Niederreiter, L., Ko, H.J., Böck, J., Martinez-Naves, E., Glickman, J.N., Tschurtschenthaler, M., Hartwig, J., Hosomi, S., et al. (2013). Paneth cells as a site of origin for intestinal inflammation. Nature *503*, 272–276. https://doi.org/10.1038/nature12599.

6. Heazlewood, C.K., Cook, M.C., Eri, R., Price, G.R., Tauro, S.B., Taupin, D., Thornton, D.J., Png, C.W., Crockford, T.L., Cornall, R.J., et al. (2008). Aberrant mucin assembly in mice causes endoplasmic reticulum stress and spontaneous inflammation resembling ulcerative colitis. PLoS Med. *5*, e54. https://doi.org/10.1371/journal.pmed.0050054.

7. Kaser, A., Lee, A.H., Franke, A., Glickman, J.N., Zeissig, S., Tilg, H., Nieuwenhuis, E.E.S., Higgins, D.E., Schreiber, S., Glimcher, L.H., and Blumberg, R.S. (2008). XBP1 links ER stress to intestinal inflammation and confers genetic risk for human inflammatory bowel disease. Cell *134*, 743–756. https://doi.org/10.1016/j.cell.2008.07.021.

8. Zhao, F., Edwards, R., Dizon, D., Afrasiabi, K., Mastroianni, J.R., Geyfman, M., Ouellette, A.J., Andersen, B., and Lipkin, S.M. (2010). Disruption of Paneth and goblet cell homeostasis and increased endoplasmic reticulum stress in Agr2-/- mice. Dev. Biol. *338*, 270–279. https://doi.org/10.1016/j.ydbio.2009.12.008.

9. Hetz, C. (2012). The unfolded protein response: controlling cell fate decisions under ER stress and beyond. Nat. Rev. Mol. Cell Biol. *13*, 89–102. https://doi.org/10.1038/nrm3270.

10. Ron, D., and Walter, P. (2007). Signal integration in the endoplasmic reticulum unfolded protein response. Nat. Rev. Mol. Cell Biol. *8*, 519–529. https://doi.org/10.1038/nrm2199.

11. Coleman, O.I., and Haller, D. (2019). ER Stress and the UPR in Shaping Intestinal Tissue Homeostasis and Immunity. Front. Immunol. *10*, 2825. https://doi.org/10.3389/fimmu.2019.02825.

12. Eugene, S.P., Reddy, V.S., and Trinath, J. (2020). Endoplasmic Reticulum Stress and Intestinal Inflammation: A Perilous Union. Front. Immunol. *11*, 543022. https://doi.org/10.3389/fimmu.2020.543022.

13. Cao, S.S. (2018). Cellular Stress Responses and Gut Microbiota in Inflammatory Bowel Disease. Gastroenterol. Res. Pract. *2018*, 7192646. https://doi.org/10.1155/2018/7192646.

14. Powell, N., Pantazi, E., Pavlidis, P., Tsakmaki, A., Li, K., Yang, F., Parker, A., Pin, C., Cozzetto, D., Minns, D., et al. (2020). Interleukin-22 orchestrates a pathological endoplasmic reticulum stress response transcriptional programme in colonic epithelial cells. Gut *69*, 578–590. https://doi.org/10.1136/gutjnl-2019-318483.

15. Vanhove, W., Nys, K., Arijs, I., Cleynen, I., Noben, M., De Schepper, S., Van Assche, G., Ferrante, M., and Vermeire, S. (2018). Biopsy-derived Intestinal Epithelial Cell Cultures for Pathway-based Stratification of Patients With Inflammatory Bowel Disease. J. Crohns Colitis *12*, 178–187. https://doi.org/10.1093/ecco-jcc/jjx122.

16. Welz, L., Kakavand, N., Hang, X., Laue, G., Ito, G., Silva, M.G., Plattner, C., Mishra, N., Tengen, F., Ogris, C., et al. (2022). Epithelial X-Box Binding Protein 1 Coordinates Tumor Protein p53-Driven DNA Damage Responses

and Suppression of Intestinal Carcinogenesis. Gastroenterology *162*, 223–237.e11. https://doi.org/10.1053/j.gastro.2021.09.057.

17. Niederreiter, L., Fritz, T.M.J., Adolph, T.E., Krismer, A.M., Offner, F.A., Tschurtschenthaler, M., Flak, M.B., Hosomi, S., Tomczak, M.F., Kaneider, N.C., et al. (2013). ER stress transcription factor Xbp1 suppresses intestinal tumorigenesis and directs intestinal stem cells. J. Exp. Med. *210*, 2041–2056. https://doi.org/10.1084/jem.20122341.

18. Benzarti, M., Delbrouck, C., Neises, L., Kiweler, N., and Meiser, J. (2020). Metabolic Potential of Cancer Cells in Context of the Metastatic Cascade. Cells *9*. https://doi.org/10.3390/cells9092035.

19. Harding, H.P., Zhang, Y., Zeng, H., Novoa, I., Lu, P.D., Calfon, M., Sadri, N., Yun, C., Popko, B., Paules, R., et al. (2003). An integrated stress response regulates amino acid metabolism and resistance to oxidative stress. Mol. Cell *11*, 619–633. https://doi.org/10.1016/s1097-2765(03)00105-9.

20. Sies, H., and Jones, D.P. (2020). Reactive oxygen species (ROS) as pleiotropic physiological signalling agents. Nat. Rev. Mol. Cell Biol. *21*, 363–383. https://doi.org/10.1038/s41580-020-0230-3.

21. Li, Z., Xu, D., Li, X., Deng, Y., and Li, C. (2022). Redox Imbalance in Chronic Inflammatory Diseases. BioMed Res. Int. *2022*, 9813486. https://doi.org/10.1155/2022/9813486.

22. Łuczaj, W., Gęgotek, A., and Skrzydlewska, E. (2017). Antioxidants and HNE in redox homeostasis. Free Radic. Biol. Med. *111*, 87–101. https://doi.org/10.1016/j.freeradbiomed.2016.11.033.

23. Jia, M., Qin, D., Zhao, C., Chai, L., Yu, Z., Wang, W., Tong, L., Lv, L., Wang, Y., Rehwinkel, J., et al. (2020). Redox homeostasis maintained by GPX4 facilitates STING activation. Nat. Immunol. *21*, 727–735. https://doi.org/10.1038/s41590-020-0699-0.

24. Motwani, M., Pesiridis, S., and Fitzgerald, K.A. (2019). DNA sensing by the cGAS-STING pathway in health and disease. Nat. Rev. Genet. *20*, 657–674. https://doi.org/10.1038/s41576-019-0151-1.

25. Hopfner, K.P., and Hornung, V. (2020). Molecular mechanisms and cellular functions of cGAS-STING signalling. Nat. Rev. Mol. Cell Biol. *21*, 501–521. https://doi.org/10.1038/s41580-020-0244-x.

26. Wottawa, F., Bordoni, D., Baran, N., Rosenstiel, P., and Aden, K. (2021). The role of cGAS/STING in intestinal immunity. Eur. J. Immunol. *51*, 785–797. https://doi.org/10.1002/eji.202048777.

27. Lio, C.W.J., McDonald, B., Takahashi, M., Dhanwani, R., Sharma, N., Huang, J., Pham, E., Benedict, C.A., and Sharma, S. (2016). cGAS-STING Signaling Regulates Initial Innate Control of Cytomegalovirus Infection. J. Virol. *90*, 7789–7797. https://doi.org/10.1128/JVI.01040-16.

28. Piersma, S.J., Poursine-Laurent, J., Yang, L., Barber, G.N., Parikh, B.A., and Yokoyama, W.M. (2020). Virus infection is controlled by hematopoietic and stromal cell sensing of murine cytomegalovirus through STING. Elife *9*, e56882. https://doi.org/10.7554/eLife.56882.

29. Stempel, M., Chan, B., Juranić Lisnić, V., Krmpotić, A., Hartung, J., Paludan, S.R., Füllbrunn, N., Lemmermann, N.A., and Brinkmann, M.M. (2019). The herpesviral antagonist m152 reveals differential activation of STING-dependent IRF and NF-kappaB signaling and STING's dual role during MCMV infection. EMBO J. *38*, e100983. https://doi.org/10.15252/embj.2018100983.

30. Guimarães, E.S., Gomes, M.T.R., Campos, P.C., Mansur, D.S., Dos Santos, A.A., Harms, J., Splitter, G., Smith, J.A., Barber, G.N., and Oliveira, S.C. (2019). Brucella abortus Cyclic Dinucleotides Trigger STING-Dependent Unfolded Protein Response That Favors Bacterial Replication. J. Immunol. *202*, 2671–2681. https://doi.org/10.4049/jimmunol.1801233.

31. Moretti, J., Roy, S., Bozec, D., Martinez, J., Chapman, J.R., Ueberheide, B., Lamming, D.W., Chen, Z.J., Horng, T., Yeretssian, G., et al. (2017). STING Senses Microbial Viability to Orchestrate Stress-Mediated Autophagy of the Endoplasmic Reticulum. Cell *171*, 809–823.e13. https://doi.org/10.1016/j.cell.2017.09.034.

32. Aden, K., Tran, F., Ito, G., Sheibani-Tezerji, R., Lipinski, S., Kuiper, J.W., Tschurtschenthaler, M., Saveljeva, S., Bhattacharyya, J., Häsler, R., et al. (2018). ATG16L1 orchestrates interleukin-22 signaling in the intestinal epithelium via cGAS-STING. J. Exp. Med. *215*, 2868–2886. https://doi.org/10.1084/jem.20171029.

33. Ma, X., Dai, Z., Sun, K., Zhang, Y., Chen, J., Yang, Y., Tso, P., Wu, G., and Wu, Z. (2017). Intestinal Epithelial Cell Endoplasmic Reticulum Stress and Inflammatory Bowel Disease Pathogenesis: An Update Review. Front. Immunol. *8*, 1271. https://doi.org/10.3389/fimmu.2017.01271.

34. Kaser, A., Martínez-Naves, E., and Blumberg, R.S. (2010). Endoplasmic reticulum stress: implications for inflammatory bowel disease pathogenesis. Curr. Opin. Gastroenterol. *26*, 318–326. https://doi.org/10.1097/MOG.0b013e32833a9ff1.

35. Zheng, W., Rosenstiel, P., Huse, K., Sina, C., Valentonyte, R., Mah, N., Zeitlmann, L., Grosse, J., Ruf, N., Nürnberg, P., et al. (2006). Evaluation of AGR2 and AGR3 as candidate genes for inflammatory bowel disease. Genes Immun. *7*, 11–18. https://doi.org/10.1038/sj.gene.6364263.

36. Parker, J.L., Deme, J.C., Kolokouris, D., Kuteyi, G., Biggin, P.C., Lea, S.M., and Newstead, S. (2021). Molecular basis for redox control by the human cystine/glutamate antiporter system xc. Nat. Commun. *12*, 7147. https://doi.org/10.1038/s41467-021-27414-1.

37. Meiser, J., Tumanov, S., Maddocks, O., Labuschagne, C.F., Athineos, D., Van Den Broek, N., Mackay, G.M., Gottlieb, E., Blyth, K., Vousden, K., et al. (2016). Serine one-carbon catabolism with formate overflow. Sci. Adv. *2*, e1601273. https://doi.org/10.1126/sciadv.1601273.

38. Labuschagne, C.F., van den Broek, N.J.F., Mackay, G.M., Vousden, K.H., and Maddocks, O.D.K. (2014). Serine, but not glycine, supports one-carbon metabolism and proliferation of cancer cells. Cell Rep. *7*, 1248–1258. https://doi.org/10.1016/j.celrep.2014.04.045.

39. Benzarti, M., Oudin, A., Viry, E., Gargiulo, E., Schmoetten, M., Neises, L., Pulido, C., Lorenz, N.I., Ronellenfitsch, M.W., Sumpton, D., et al. (2023). PKM2 diverts glycolytic flux in dependence on mitochondrial one-carbon cycle. Preprint at bioRxiv *8*. https://doi.org/10.1101/2023.01.23.525168.

40. Liu, Y., Adachi, M., Zhao, S., Hareyama, M., Koong, A.C., Luo, D., Rando, T.A., Imai, K., and Shinomura, Y. (2009). Preventing oxidative stress: a new role for XBP1. Cell Death Differ. *16*, 847–857. https://doi.org/10.1038/cdd.2009.14.

41. Yu, S., Gao, L., Song, Y., Ma, X., Liang, S., Lan, H., Zheng, X., and Li, S. (2021). Glycine ameliorates mitochondrial dysfunction caused by ABT-199 in porcine oocytes. J. Anim. Sci. *99*, skab072. https://doi.org/10.1093/jas/skab072.

42. Shi, Y., Wang, Q., Hou, Y., Hong, Y., Han, X., Yi, J., Qu, J., and Lu, Y. (2014). Molecular cloning, expression and enzymatic characterization of glutathione S-transferase from Antarctic sea-ice bacteria Pseudoalteromonas sp. ANT506. Microbiol. Res. *169*, 179–184. https://doi.org/10.1016/j.micres.2013.06.012.

43. Tajan, M., Hennequart, M., Cheung, E.C., Zani, F., Hock, A.K., Legrave, N., Maddocks, O.D.K., Ridgway, R.A., Athineos, D., Suárez-Bonnet, A., et al. (2021). Serine synthesis pathway inhibition cooperates with dietary serine and glycine limitation for cancer therapy. Nat. Commun. *12*, 366. https://doi.org/10.1038/s41467-020-20223-y.

44. Weinstabl, H., Treu, M., Rinnenthal, J., Zahn, S.K., Ettmayer, P., Bader, G., Dahmann, G., Kessler, D., Rumpel, K., Mischerikow, N., et al. (2019). Intracellular Trapping of the Selective Phosphoglycerate Dehydrogenase (PHGDH) Inhibitor BI-4924 Disrupts Serine Biosynthesis. J. Med. Chem. *62*, 7976–7997. https://doi.org/10.1021/acs.jmedchem.9b00718.

45. Kiweler, N., Delbrouck, C., Pozdeev, V.I., Neises, L., Soriano-Baguet, L., Eiden, K., Xian, F., Benzarti, M., Haase, L., Koncina, E., et al. (2022). Mitochondria preserve an autarkic one-carbon cycle to confer growth-independent cancer cell migration and metastasis. Nat. Commun. *13*, 2699. https://doi.org/10.1038/s41467-022-30363-y.

46. Häsler, R., Sheibani-Tezerji, R., Sinha, A., Barann, M., Rehman, A., Esser, D., Aden, K., Knecht, C., Brandt, B., Nikolaus, S., et al. (2017). Uncoupling of mucosal gene regulation, mRNA splicing and adherent microbiota signatures in inflammatory bowel disease. Gut *66*, 2087–2097. https://doi.org/10.1136/gutjnl-2016-311651.

47. Haberman, Y., Karns, R., Dexheimer, P.J., Schirmer, M., Somekh, J., Jurickova, I., Braun, T., Novak, E., Bauman, L., Collins, M.H., et al. (2019). Ulcerative colitis mucosal transcriptomes reveal mitochondriopathy and personalized mechanisms underlying disease severity and treatment response. Nat. Commun. *10*, 38. https://doi.org/10.1038/s41467-018-07841-3.

48. Arijs, I., De Hertogh, G., Lemmens, B., Van Lommel, L., de Bruyn, M., Vanhove, W., Cleynen, I., Machiels, K., Ferrante, M., Schuit, F., et al. (2018). Effect of vedolizumab (anti-alpha4beta7-integrin) therapy on histological healing and mucosal gene expression in patients with UC. Gut *67*, 43–52. https://doi.org/10.1136/gutjnl-2016-312293.

49. Sæterstad, S., Østvik, A.E., Røyset, E.S., Bakke, I., Sandvik, A.K., and Granlund, A.V.B. (2022). Profound gene expression changes in the epithelial monolayer of active ulcerative colitis and Crohn's disease. PLoS One *17*, e0265189. https://doi.org/10.1371/journal.pone.0265189.

50. Duan, J., Matute, J.D., Unger, L.W., Hanley, T., Schnell, A., Lin, X., Krupka, N., Griebel, P.,

Lambden, C., Sit, B., et al. (2023). Endoplasmic reticulum stress in the intestinal epithelium initiates purine metabolite synthesis and promotes Th17 cell differentiation in the gut. Immunity 56, 1115–1131.e9. https://doi.org/10.1016/j.immuni.2023.02.018.

51. Smillie, C.S., Biton, M., Ordovas-Montanes, J., Sullivan, K.M., Burgin, G., Graham, D.B., Herbst, R.H., Rogel, N., Slyper, M., Waldman, J., et al. (2019). Intra- and Inter-cellular Rewiring of the Human Colon during Ulcerative Colitis. Cell 178, 714–730.e22. https://doi.org/10.1016/j.cell.2019.06.029.

52. Irving, P.M., de Lusignan, S., Tang, D., Nijher, M., and Barrett, K. (2021). Risk of common infections in people with inflammatory bowel disease in primary care: a population-based cohort study. BMJ Open Gastroenterol. 8, e000573. https://doi.org/10.1136/bmjgast-2020-000573.

53. Isler, J.A., Skalet, A.H., and Alwine, J.C. (2005). Human cytomegalovirus infection activates and regulates the unfolded protein response. J. Virol. 79, 6890–6899. https://doi.org/10.1128/JVI.79.11.6890-6899.2005.

54. Tao, L., Lemoff, A., Wang, G., Zarek, C., Lowe, A., Yan, N., and Reese, T.A. (2020). Reactive oxygen species oxidize STING and suppress interferon production. Elife 9, e57837. https://doi.org/10.7554/eLife.57837.

55. Marinho, F.V., Benmerzoug, S., Oliveira, S.C., Ryffel, B., and Quesniaux, V.F.J. (2017). The Emerging Roles of STING in Bacterial Infections. Trends Microbiol. 25, 906–918. https://doi.org/10.1016/j.tim.2017.05.008.

56. Coleman, O.I., Lobner, E.M., Bierwirth, S., Sorbie, A., Waldschmitt, N., Rath, E., Berger, E., Lagkouvardos, I., Clavel, T., McCoy, K.D., et al. (2018). Activated ATF6 Induces Intestinal Dysbiosis and Innate Immune Response to Promote Colorectal Tumorigenesis. Gastroenterology 155, 1539–1552.e12. https://doi.org/10.1053/j.gastro.2018.07.028.

57. Stengel, S., Messner, B., Falk-Paulsen, M., Sommer, N., and Rosenstiel, P. (2017). Regulated proteolysis as an element of ER stress and autophagy: Implications for intestinal inflammation. Biochim. Biophys. Acta. Mol. Cell Res. 1864, 2183–2190. https://doi.org/10.1016/j.bbamcr.2017.07.008.

58. Yin, X., Farin, H.F., van Es, J.H., Clevers, H., Langer, R., and Karp, J.M. (2014). Niche-independent high-purity cultures of Lgr5+ intestinal stem cells and their progeny. Nat. Methods 11, 106–112. https://doi.org/10.1038/nmeth.2737.

59. Dambacher, J., Beigel, F., Seiderer, J., Haller, D., Göke, B., Auernhammer, C.J., and Brand, S. (2007). Interleukin 31 mediates MAP kinase and STAT1/3 activation in intestinal epithelial cells and its expression is upregulated in inflammatory bowel disease. Gut 56, 1257–1265. https://doi.org/10.1136/gut.2006.118679.

60. Onyeagocha, C., Hossain, M.S., Kumar, A., Jones, R.M., Roback, J., and Gewirtz, A.T. (2009). Latent cytomegalovirus infection exacerbates experimental colitis. Am. J. Pathol. 175, 2034–2042. https://doi.org/10.2353/ajpath.2009.090471.

61. Hansen, K., Prabakaran, T., Laustsen, A., Jørgensen, S.E., Rahbæk, S.H., Jensen, S.B., Nielsen, R., Leber, J.H., Decker, T., Horan, K.A., et al. (2014). Listeria monocytogenes induces IFNbeta expression through an IFI16-cGAS- and STING-dependent pathway.

EMBO J. 33, 1654–1666. https://doi.org/10.15252/embj.201488029.

62. Peterson, L.W., and Artis, D. (2014). Intestinal epithelial cells: regulators of barrier function and immune homeostasis. Nat. Rev. Immunol. 14, 141–153. https://doi.org/10.1038/nri3608.

63. DeBerardinis, R.J., and Chandel, N.S. (2016). Fundamentals of cancer metabolism. Sci. Adv. 2, e1600200. https://doi.org/10.1126/sciadv.1600200.

64. Kaser, A., and Blumberg, R.S. (2010). Endoplasmic reticulum stress and intestinal inflammation. Mucosal Immunol. 3, 11–16. https://doi.org/10.1038/mi.2009.122.

65. Howard, A., Tahir, I., Javed, S., Waring, S.M., Ford, D., and Hirst, B.H. (2010). Glycine transporter GLYT1 is essential for glycine-mediated protection of human intestinal epithelial cells against oxidative damage. J. Physiol. 588, 995–1009. https://doi.org/10.1113/jphysiol.2009.186262.

66. Gonen, N., Meller, A., Sabath, N., and Shalgi, R. (2019). Amino Acid Biosynthesis Regulation during Endoplasmic Reticulum Stress Is Coupled to Protein Expression Demands. iScience 19, 204–213. https://doi.org/10.1016/j.isci.2019.07.022.

67. Diehl, F.F., Lewis, C.A., Fiske, B.P., and Vander Heiden, M.G. (2019). Cellular redox state constrains serine synthesis and nucleotide production to impact cell proliferation. Nat. Metab. 1, 861–867. https://doi.org/10.1038/s42255-019-0108-x.

68. Niu, X., Stancliffe, E., Gelman, S.J., Wang, L., Schwaiger-Haber, M., Rowles, J.L., 3rd, Shriver, L.P., and Patti, G.J. (2023). Cytosolic and mitochondrial NADPH fluxes are independently regulated. Nat. Chem. Biol. 19, 837–845. https://doi.org/10.1038/s41589-023-01283-9.

69. Hennequart, M., Pilley, S.E., Labuschagne, C.F., Coomes, J., Mervant, L., Driscoll, P.C., Legrave, N.M., Lee, Y., Kreuzaler, P., Macintyre, B., et al. (2023). ALDH1L2 regulation of formate, formyl-methionine, and ROS controls cancer cell migration and metastasis. Cell Rep. 42, 112562. https://doi.org/10.1016/j.celrep.2023.112562.

70. Fan, J., Ye, J., Kamphorst, J.J., Shlomi, T., Thompson, C.B., and Rabinowitz, J.D. (2014). Quantitative flux analysis reveals folate-dependent NADPH production. Nature 510, 298–302. https://doi.org/10.1038/nature13236.

71. Piskounova, E., Agathocleous, M., Murphy, M.M., Hu, Z., Huddlestun, S.E., Zhao, Z., Leitch, A.M., Johnson, T.M., DeBerardinis, R.J., and Morrison, S.J. (2015). Oxidative stress inhibits distant metastasis by human melanoma cells. Nature 527, 186–191. https://doi.org/10.1038/nature15726.

72. Ducker, G.S., Chen, L., Morscher, R.J., Ghergurovich, J.M., Esposito, M., Teng, X., Kang, Y., and Rabinowitz, J.D. (2016). Reversal of Cytosolic One-Carbon Flux Compensates for Loss of the Mitochondrial Folate Pathway. Cell Metab. 24, 640–641. https://doi.org/10.1016/j.cmet.2016.09.011.

73. Quirós, P.M., Prado, M.A., Zamboni, N., D'Amico, D., Williams, R.W., Finley, D., Gygi, S.P., and Auwerx, J. (2017). Multi-omics analysis identifies ATF4 as a key regulator of the mitochondrial stress response in mammals. J. Cell Biol. 216, 2027–2045. https://doi.org/10.1083/jcb.201702058.

74. van der Mijn, J.C., Chen, Q., Laursen, K.B., Khani, F., Wang, X., Dorsaint, P., Sboner, A., Gross, S.S., Nanus, D.M., and Gudas, L.J.

(2022). Transcriptional and metabolic remodeling in clear cell renal cell carcinoma caused by ATF4 activation and the integrated stress response (ISR). Mol. Carcinog. 61, 851–864. https://doi.org/10.1002/mc.23437.

75. Ryan, D.G., Yang, M., Prag, H.A., Blanco, G.R., Nikitopoulou, E., Segarra-Mondejar, M., Powell, C.A., Young, T., Burger, N., Miljkovic, J.L., et al. (2021). Disruption of the TCA cycle reveals an ATF4-dependent integration of redox and amino acid metabolism. Elife 10, e72593. https://doi.org/10.7554/eLife.72593.

76. Han, J., Back, S.H., Hur, J., Lin, Y.H., Gildersleeve, R., Shan, J., Yuan, C.L., Krokowski, D., Wang, S., Hatzoglou, M., et al. (2013). ER-stress-induced transcriptional regulation increases protein synthesis leading to cell death. Nat. Cell Biol. 15, 481–490. https://doi.org/10.1038/ncb2738.

77. Balsa, E., Soustek, M.S., Thomas, A., Cogliati, S., Garcia-Poyatos, C., Martin-Garcia, E., Jedrychowski, M., Gygi, S.P., Enriquez, J.A., and Puigserver, P. (2019). ER and Nutrient Stress Promote Assembly of Respiratory Chain Supercomplexes through the PERK-eIF2alpha Axis. Mol Cell 74, 877–890. https://doi.org/10.1016/j.molcel.2019.03.031.

78. Guan, B.J., Krokowski, D., Majumder, M., Schmotzer, C.L., Kimball, S.R., Merrick, W.C., Koromilas, A.E., and Hatzoglou, M. (2014). Translational control during endoplasmic reticulum stress beyond phosphorylation of the translation initiation factor eIF2alpha. J. Biol. Chem. 289, 12593–12611. https://doi.org/10.1074/jbc.M113.543215.

79. Seibt, T.M., Proneth, B., and Conrad, M. (2019). Role of GPX4 in ferroptosis and its pharmacological implication. Free Radic. Biol. Med. 133, 144–152. https://doi.org/10.1016/j.freeradbiomed.2018.09.014.

80. Mayr, L., Grabherr, F., Schwärzler, J., Reitmeier, I., Sommer, F., Gehmacher, T., Niederreiter, L., He, G.W., Ruder, B., Kunz, K.T.R., et al. (2020). Dietary lipids fuel GPX4-restricted enteritis resembling Crohn's disease. Nat. Commun. 11, 1775. https://doi.org/10.1038/s41467-020-15646-6.

81. Heijmans, J., van Lidth de Jeude, J.F., Koo, B.K., Rosekrans, S.L., Wielenga, M.C.B., van de Wetering, M., Ferrante, M., Lee, A.S., Onderwater, J.J.M., Paton, J.C., et al. (2013). ER stress causes rapid loss of intestinal epithelial stemness through activation of the unfolded protein response. Cell Rep. 3, 1128–1139. https://doi.org/10.1016/j.celrep.2013.02.031.

82. Thavamani, A., Umapathi, K.K., Sferra, T.J., and Sankararaman, S. (2023). Cytomegalovirus Infection Is Associated With Adverse Outcomes Among Hospitalized Pediatric Patients With Inflammatory Bowel Disease. Gastroenterology Res. 16, 1–8. https://doi.org/10.14740/gr1588.

83. Mavropoulou, E., Ternes, K., Mechie, N.C., Bremer, S.C.B., Kunsch, S., Ellenrieder, V., Neesse, A., and Amanzada, A. (2019). Cytomegalovirus colitis in inflammatory bowel disease and after haematopoietic stem cell transplantation: diagnostic accuracy, predictors, risk factors and disease outcome. BMJ Open Gastroenterol. 6, e000258. https://doi.org/10.1136/bmjgast-2018-000258.

84. Paiva, C.N., and Bozza, M.T. (2014). Are reactive oxygen species always detrimental to pathogens? Antioxid. Redox Signal. 20, 1000–1037. https://doi.org/10.1089/ars.2013.5447.

85. Ye, F., Zhou, F., Bedolla, R.G., Jones, T., Lei, X., Kang, T., Guadalupe, M., and Gao, S.J. (2011). Reactive oxygen species hydrogen peroxide mediates Kaposi's sarcoma-associated herpesvirus reactivation from latency. PLoS Pathog. 7, e1002054. https://doi.org/10.1371/journal.ppat.1002054.

86. Fisher, M.A., and Lloyd, M.L. (2020). A Review of Murine Cytomegalovirus as a Model for Human Cytomegalovirus Disease-Do Mice Lie? Int. J. Mol. Sci. 22, 214. https://doi.org/10.3390/ijms22010214.

87. Crawford, L.B., Streblow, D.N., Hakki, M., Nelson, J.A., and Caposio, P. (2015). Humanized mouse models of human cytomegalovirus infection. Curr. Opin. Virol. 13, 86–92. https://doi.org/10.1016/j.coviro.2015.06.006.

88. Madison, B.B., Dunbar, L., Qiao, X.T., Braunstein, K., Braunstein, E., and Gumucio, D.L. (2002). Cis elements of the villin gene control expression in restricted domains of the vertical (crypt) and horizontal (duodenum, cecum) axes of the intestine. J. Biol. Chem. 277, 33275–33283. https://doi.org/10.1074/jbc.M204935200.

89. Jin, L., Hill, K.K., Filak, H., Mogan, J., Knowles, H., Zhang, B., Perraud, A.L., Cambier, J.C., and Lenz, L.L. (2011). MPYS is required for IFN response factor 3 activation and type I IFN production in the response of cultured phagocytes to bacterial second messengers cyclic-di-AMP and cyclic-di-GMP. J. Immunol. 187, 2595–2601. https://doi.org/10.4049/jimmunol.1100088.

90. Lee, A.H., Iwakoshi, N.N., Anderson, K.C., and Glimcher, L.H. (2003). Proteasome inhibitors disrupt the unfolded protein response in myeloma cells. Proc. Natl. Acad. Sci. USA 100, 9946–9951. https://doi.org/10.1073/pnas.1334037100.

91. Sato, T., Vries, R.G., Snippert, H.J., van de Wetering, M., Barker, N., Stange, D.E., van Es, J.H., Abo, A., Kujala, P., Peters, P.J., and Clevers, H. (2009). Single Lgr5 stem cells build crypt-villus structures in vitro without a mesenchymal niche. Nature 459, 262–265. https://doi.org/10.1038/nature07935.

92. Chan, B., Gonçalves Magalhães, V., Lemmermann, N.A.W., Juranić Lisnić, V., Stempel, M., Bussey, K.A., Reimer, E., Podlech, J., Lienenklaus, S., Reddehase, M.J., et al. (2017). The murine cytomegalovirus M35 protein antagonizes type I IFN induction downstream of pattern recognition receptors by targeting NF-kappaB mediated transcription. PLoS Pathog. 13, e1006382. https://doi.org/10.1371/journal.ppat.1006382.

93. Sorbara, M.T., Ellison, L.K., Ramjeet, M., Travassos, L.H., Jones, N.L., Girardin, S.E., and Philpott, D.J. (2013). The protein ATG16L1 suppresses inflammatory cytokines induced by the intracellular sensors Nod1 and Nod2 in an autophagy-independent manner. Immunity 39, 858–873. https://doi.org/10.1016/j.immuni.2013.10.013.

94. Foroutan, M., Bhuva, D.D., Lyu, R., Horan, K., Cursons, J., and Davis, M.J. (2018). Single sample scoring of molecular phenotypes. BMC Bioinf. 19, 404. https://doi.org/10.1186/s12859-018-2435-4.

95. Bhuva, D.D., Cursons, J., and Davis, M.J. (2020). Stable gene expression for normalisation and single-sample scoring. Nucleic Acids Res. 48, e113. https://doi.org/10.1093/nar/gkaa802.

96. Hiller, K., Hangebrauk, J., Jäger, C., Spura, J., Schreiber, K., and Schomburg, D. (2009). MetaboliteDetector: comprehensive analysis tool for targeted and nontargeted GC/MS based metabolome analysis. Anal. Chem. 81, 3429–3439. https://doi.org/10.1021/ac802689c.

98. Till, A., Rosenstiel, P., Bräutigam, K., Sina, C., Jacobs, G., Oberg, H-H., Seegert, D., Chakraborty, T., and Schreiber, S. (2008). A role for membrane-bound CD147 in NOD2-mediated recognition of bacterial cytoinvasion. J. Cell Sci. 15, 487–495. https://doi.org/10.1242/jcs.016980.

99. Cicin-Sain, L., Podlech, J., Messerle, M., Reddehase, M.J., and Koszinowski, U.H. (2005). Frequent coinfection of cells explains functional in vivo complementation between cytomegalovirus variants in the multiply infected host. J. Virol. 79, 9492–9502. https://doi.org/10.1128/JVI.79.15.9492-9502.2005.

STAR★METHODS

KEY RESOURCES TABLE

REAGENT or RESOURCE	SOURCE	IDENTIFIER
Antibodies		
β-Actin (8H10D10) Mouse mAb	Cell Signaling Technology	Cat# 3700; RRID:AB_2242334
β-Actin	Sigma-Aldrich,	Cat# A-5441
Tubulin	MBL International,	Cat# M150-3
Vinculin	Cell Signaling Technology	Cat# 13901
Aldh1l2	Sigma-Aldrich,	HPA039481
phosphoSting	Cell Signaling Technology	Cat# 72971
STING	Cell Signaling Technology	Cat# 13647
phosphoTBK1	Cell Signaling Technology	Cat# 5483
TBK1	Cell Signaling Technology	Cat# 38066
Mouse-HRP	Amersham Biosciences	Cat# NA931V
Rabbit-HRP	Amersham Biosciences	Cat# NA934V
rabbit-IRDye® 800CW	LiCOR Technologies	Cat# 926-32213
Mouse-IRDye® 680CW	LiCOR Technologies	Cat# 926-68070
Lysozyme	Cell Signaling Technology	Cat# 60487
Chemicals, peptides, and recombinant proteins		
Custom-made DMEM without Ser/Gly based on Cat# A1443001	Gibco	n/a
Serine	Sigma-Aldrich	S4500
Glycine	Sigma-Aldrich	50046
[U-13C]-glucose tracer	Cambridge Isotope Laboratories	CLM-1396
[U-13C]-glutamine tracer	Cambridge Isotope Laboratories	CLM-1822
RSL3	Selleck Cehmicals	S8155
BI-4916	MedChemExpress	HY-126253
NAC	Sigma Aldrich	A7250-25G
DMXAA	MedChemExpress	HY-10964
Tunicamycin	Sigma-Aldrich	T7765-1MG
Tamoxifen	Sigma Aldrich	T2859
FBS	Sigma Aldrich	F0392-100ML
Matrigel	Corning	356234
Corning™ Cell Recovery Solution	Corning	354253
Zombie-NIR	Biolegend	423105
DCF-DA	Sigma Aldrich	D6883
Critical commercial assays		
RNeasy Mini Kit	Qiagen	74104
Maxima H Minus First Strand cDNA Synthesis Kit	Thermo Fisher Scientific	K1652
High-capacity cDNA Reverse Transcription Kit	Thermo Fisher Scientific	4368814
Fast SYBR™ Green Master Mix	Thermo Fisher Scientific	4385612
GSH/GSSG-GLO™ assay kit	Promega	V6611
Viromer® Blue kit	Lipocalyx	VB-01LB-00
NADP/NADPH Assay Kit	Abcam	ab65349
Image-iT™ Lipid Peroxidation Kit	Thermo Fisher Scientific	C10445

(Continued on next page)

Continued

REAGENT or RESOURCE	SOURCE	IDENTIFIER
Bacterial and virus strains		
Listeria monocytogenes serotype 1/2a strain EGD	Philip Rosenstiel	Till et al.[98]
MCMV	Luka Cicin-Sain	Cicin-Sain et al.[99]
Experimental models: Organisms/strains		
Villin-Cre nAtf6[IEC] mice (nAtf6 VilCreERT2 transgene (tg))	Dirk Haller	Coleman et al.[56]
Tmem173^{-/-} mice	Jackson Laboratory	strain #025805
Xbp1^{fl/fl} mice	Arthur Kaser	Niederreiter et al.[17]
Xbp1[ΔIEC] mice	Arthur Kaser	Niederreiter et al.[17]
Experimental models: cell lines		
Mode-K iCtrl	Arthur Kaser	Kaser et al.[7]
Mode-K iXbp1	Arthur Kaser	Kaser et al.[7]
Oligonucleotides		
Tagman assay probe *Cxcl10*	Life Technologies	04331182
Tagman assay probe *Tmem173*	Life Technologies	01158117
Tagman assay probe *Ifnb1*	Life Technologies	04331182
Tagman assay probe *Gapdh*	Life Technologies	99999915
Tagman assay probe *Xbp1*	Life Technologies	03464496
Tagman assay probe *Shmt1*	Integrated DNA Technologies	Shmt1 NM_009171(1)
Tagman assay probe *Shmt2*	Integrated DNA Technologies	Shmt2 NM_001252316(2)
Tagman assay probe *Aldh1l1*	Integrated DNA Technologies	Aldh1l1 NM_027406(1)
Tagman assay probe *Aldh1l2*	Integrated DNA Technologies	Aldh1l2 NM_153543(1)
Tagman assay probe *Mthfd1*	Integrated DNA Technologies	Mthfd1 NM_138745(1)
Tagman assay probe *Mthfd2*	Integrated DNA Technologies	Mthfd2 NM_008638(1)
Tagman assay probe *Psat1*	Integrated DNA Technologies	Psat1 NM_001205339(2)
Tagman assay probe *Psph*	Integrated DNA Technologies	Psph NM_133900(1)
Tagman assay probe *Phgdh*	Integrated DNA Technologies	Phghd NM_016966(1)
Tagman assay probe *Actb1*	Integrated DNA Technologies	Actb NM_007393(1)
BIP FW: 5′- TGTCTTCTCAGCATCAAGCAAGG -3′ *BIP* RV: 5′- CCAACACTTCCTGGACAGGCTT -3′	Eurogentec	N/A
Slc7a11 Fw: 5′- GCTCGTAATACGCCCTGGAG -3′ *Slc7a11* Rv: 5′- GGAAAATCTGGATCCGGGCA -3′	Eurogentec	N/A
Gpx1 Fw: 5′- ACCGTGTATGCCTTCTCCGC -3′ *Gpx1* Rv: 5′- CTCGGTGTAGTCCCGGATCG -3′	Eurogentec	N/A
Gpx2 Fw: 5′- AGTTCGGACATCAGGAGAACTG -3′ *Gpx2* Rv: 5′- GATGCTCGTTCTGCCCATTG -3′	Eurogentec	N/A
Gpx3 Fw: 5′- ACAATTGTCCCAGTGTGTGCAT -3′ *Gpx3* Rv: 5′- TGGACCATCCCTGGGTTTC -3′	Eurogentec	N/A
Gpx4 Fw: 5′- CATTGGTCGGCTGCGTGA -3′ *Gpx4* Rv: 5′- CGCGGGATGCACACATGG -3′	Eurogentec	N/A
Tbp Fw: 5′- GTCATTTTCTCCGCAGTGCC -3′ *Tbp* Rv: 5′- GCTGTTGTTCTGGTCCATGAT -3′	Eurogentec	N/A
Hrpt1 Fw: 5′- TGGATACAGGCCAGACTTTGTT -3′ *Hrpt1* Rv: 5′- CAGATTCAACTTGCGCTCATC -3′	Eurogentec	N/A
gB Fw: 5′- CTGGGCGAGAACAACGAGAT -3′ *gB* Rv: 5′- CGCAGCTCTCCCTTCGAGTA -3′	Eurogentec	N/A

Continued		
REAGENT or RESOURCE	**SOURCE**	**IDENTIFIER**
M54 Fw: 5'- ATCATCCGTTGCATCTCGTTG -3' *M54* Rv: 5'- CGCCATCTGTATCCGTCCAT -3'	Eurogentec	N/A
siRNA Tmem173	Qiagen	Cat# GS72512
Software and algorithms		
Prism	GraphPad Software	Version 5
QuantStudio Design&Analysis v1.5.1 software	Applied Biosciences, ThermoFisher Scientific	www.thermofisher.com
IncuCyte® Live-Cell Analysis system	Essen Bioscience	https://www.sartorius.com/en/products/live-cell-imaging-analysis
ImageStudioLite Software Vers.5.2	LI-COR	https://www.licor.com/bio/image-studio-lite/
Tracefinder 4.1 Software	Thermo Fisher Scientific	https://www.thermofisher.com/order/catalog/product/OPTON-31001
R version 4.2.2 (Seurat and singscore packages)	R project	https://www.r-project.org/
MetaboliteDetector software package (v. 3.220180913)	Karsten Hiller	Hiller et al.[96]
Biorender	Biorender	https://www.biorender.com/
FlowJo v10.6.2 software	BD	https://www.flowjo.com/
AxioVision Rel 4.9 software	Zeiss	https://www.micro-shop.zeiss.com/en/us/softwarefinder/

RESOURCE AVAILABILITY

Lead contact

Further information and requests for resources and reagents should be directed to and will be fulfilled by the lead contact, Konrad Aden (k.aden@ikmb.uni-kiel.de).

Materials availability

This study did not generate new unique reagents.

Data and code availability

- This paper analyses existing, publicly available data. All RNAseq data were downloaded from GEO or the editor's website. The specific accession numbers are listed in the material and method section.
- This paper does not report original code.
- Any additional information required to reanalyse the data reported in this paper is available from the lead contact upon request.

EXPERIMENTAL MODEL AND STUDY PARTICIPANT DETAILS

Mice

Xbp1^fl/fl^ mice were generated by targeted insertion of *LoxP* sites flanking the exon 2 of the *Xbp1* gene. VillinCre^+/−^ mice (strain: B6.SJL-Tg (Vil-cre)997Gum/J) were purchased from Jackson Laboratory. Conditional knockout of *Xbp1* in the intestinal epithelium was then established by crossing VillinCre^+/−^ mice with *Xbp1*^fl/fl^ mice, resulting in specific deletion of *Xbp1* (*Xbp1*^ΔIEC^) in the intestinal epithelium.[88] Tamoxifen-inducible nATF6-HA overexpressing Villin-Cre n*Atf6*^IEC^ mice (n*Atf6* VilCreERT2 transgene (tg)) mice were generated as described previously.[56] Overexpression of nATF6-HA was induced using Tamoxifen for seven days, and mice were sacrificed after another 4days allowing for full induction of overexpression. *Tmem173*^−/−^ mice were purchased from Jackson Laboratory (previously described by Jin et al., 2011, strain #025805).[89] Mice were housed under specific pathogen-free (SPF) conditions in individually ventilated cages (IVCs). Animals were held in a 12h light-dark cycle at 21°C ± 2°C and 60% ± 5% humidity. Food and water were available *ad libitum.* All animal experiments were approved by federal authorities and performed in accordance to institutional guidelines.

Cell lines

In this study, the SV40 large T-antigen-immortalised murine small intestinal epithelial cell line Mode-K (51) was employed as an *in vitro* model for the intestinal epithelium. Mode-K cells harboring an RNA interference (RNAi) based knockdown of *Xbp1* and a control RNA interference

(*iXbp1*, iCtrl) were kindly gifted by Artur Kaser, University of Cambridge.[7] In brief, RNA interference was achieved by stable introduction of a small hairpin RNA specific for *Xbp1* and a control small hairpin RNA identical to,[90] except that SFGΔU3hygro was used. Knockdown of *Xbp1* was confirmed by qRT-PCR.

Organoid generation

Mouse organoids were cultivated as described previously.[58,91] To generate sustainable cultures of small intestinal organoids, mice were sacrificed and the small intestine was removed and cut into pieces. PBS with 10 nM EDTA (Sigma Aldrich, E4884) was added to the pieces for 10 min and the specimen was placed under mild agitation. Afterward, the supernatant was removed, fresh PBS/EDTA solution was added and incubated under mild agitation for 10 min again. This was repeated four times. To remove debris, the suspension was filtered through a 100 μm strainer (Corning, 431752) and centrifuged at 1200 rpm for 10 min. Crypts were then either used for protein respectively RNA isolation or resuspended in Matrigel (Corning, 356234) and embedded in 24-well plates to generate organoid cultures. Medium was changed twice per week. Organoids were stimulated after 5 to 7 days of cultivation.

METHOD DETAILS

Chemicals and siRNA-mediated knockdown

The following chemical stimulants were used (name, company, catalogue-number): DMXAA/Vadimezan (MedChemExpress, HY-10964), N Acetyl-L-cystein (Sigma Aldrich, A7250-25G), BI-4916 (MedChemExpress, HY-126253), RSL3 (Selleck Chemicals, S8155). siRNA knockdown of *Tmem173* was performed using the Viromer Blue kit (Lipocalyx, Halle, Germany) according to the manufacturer's protocol. *Tmem173* siRNA was purchased from Qiagen (Cat # GS72512).

Cell culture

Mode-K cells were cultured in Dulbecco's modified Eagle's medium (DMEM) without phenol red, glucose, and glutamine (Thermo Fisher Scientific) and supplemented with 2 mM glutamine, 17 mM glucose, and 10% fetal bovine serum (FBS) at 37°C and 5% CO_2. For serine/glycine starvation experiments cells were kept in customised DMEM medium (Gibco) supplemented with or without 400 μM glycine and serine, 2 mM glutamine, 17 mM glucose and 10% dialyzed FBS.

In vivo MCMV infection

For *in vivo* MCMV infection, 8 week old *Xbp1*^fl/fl and *Xbp1*^ΔIEC mice were infected intraperitoneally with either 10^5 PFU MCMV or with vehicle. During the infection mice were fed a standard chow diet and had free access to food and water. Five days after infection mice were sacrificed and the intestines were harvested.

In vitro MCMV infection and quantification of replication

MCMV was prepared as described previously[92] and infection of Mode-K cells was performed at a MOI of 10. Fold induction of MCMV was quantified by qRT-PCR using the MCMV M54 or glycoprotein B (gB) gene sequence. M54: ATCATCCGTTGCATCTCGTTG (forward), CGCCATCTGTATCCGTCCAT (reverse) and gB: CTGGGCGAGAACAACGAGAT (forward), CGCAGCTCTCCCTTCGAGTA (reverse).

Histology

After sacrifice, the small intestine was removed and immediately fixed in 10% (w/v) formalin (Sigma Aldrich, HT501128) for 24 h at 4°C. The tissue was then immersed in a series of ethanol solutions of increasing concentrations until 100%. Next, the ethanol was gradually replaced with xylene, which is then replaced by paraffin. Paraffin embedded tissue was cut into 3.5–4.5 μm thin sections using the RM2255 microtome (Leica Biosystems). Paraffin embedded tissue sections were stained for 2–5 min in haematoxylin (Sigma Aldrich, H9627). The cytoplasm was counterstained with 1% (v/v) eosin solution for 2 min (Sigma Aldrich, HT110216). Stained slides were then dehydrated and embedded in Roti-Histo-Kit mounting medium (Carl Roth, 6638.1) and examined with a Zeiss AxioImager.Z1 apotome microscope (Zeiss) and the AxioVision Rel 4.9 software (Zeiss).

Histology score CMV colitis

After staining, an expert pathologist assessed inflammation with a semi quantitative scoring system as previously reported.[5] To assess the inflammation five subscores are summed up for every sample and multiplied by the extent of the affected area (1, <10%; 2, 10%–25%; 3, 25%–50%; 4, >50% of the intestine affected). As sub-scores the following parameters are used: mononuclear infiltrate (0: absent; 1: mild, 2: moderate 3: severe), crypt hyperplasia, epithelial injury/erosion, polymorphonuclear infiltrate and transmural inflammation.

Listeria monocytogenes infection

Listeria monocytogenes serotype 1/2a strain EGD was used to test type I IFN induction in Mode-K cells. Bacteria were plated out from glycerol stocks onto brain-heart infusion (BHI; BD Biosciences, USA) agar plates overnight. *Listeria* colonies were then transferred into 1 mL BHI medium and incubated overnight at 37°C to allow for bacterial replication. Next, bacteria were diluted and reincubated at 37°C to induce

a log-phase growth until OD600 = 0.6 was reached. After washing with PBS, bacteria were diluted in Mode-K medium and added to the cells according to multiciply of infection (MOI). As described previously,[93] Mode-K cells were infected at a MOI of 50. After allowing bacterial invasion for 1h, the bacteria-containing medium was removed, cells were washed once with PBS and then treated with gentamicin (50 μg/mL) for 1h to kill extracellular bacteria. The gentamicin-containing medium was then replaced with medium containing a lower concentration of Gentamicin (5 μg/mL, Sigma Aldrich, G1264), and cells were lysed for protein and RNA harvesting after another 22h.

STING immunohistochemistry and quantification

To quantify STING expression in the intestinal epithelium, 3,3′-Diaminobenizidine staining was performed. Slides were rehydrated and boiled for 20 min in citrate buffer (pH 6.0) for antigen retrieval. Unspecific binding sites were blocked by incubating slides with 5% (v/v) goat serum in phosphate-buffered saline (PBS). Naturally occurring peroxidases were inactivated by applying 3% hydrogen peroxide. Antibody binding and 3,3′-diaminobenzidine staining was performed according to the manufacturer's instruction (Vectastain Elite ABC Kit, Vector Labs, Peterborough, United Kingdom). In brief, after primary antibody binding, the signal was amplified by adding a horseradish peroxidase-conjugated streptavidin antibody. Quantification was performed by counting average STING positive cells per crypt. For each animal, 50 crypts were counted and averaged.

Cell growth analysis

Cell growth was determined as measurement of the cell density (confluence) using the IncuCyte Live-Cell Analysis system (Essen Bioscience) and following the manufacturer's instructions. In brief, 5×10^4 cells were seeded in 96 well plates as technical replicates (N = 6) and cultivated in DMEM for the indicated time period. After cell attachment, images were generated every 2h and the cell density was analyzed using the IncuCyte analysis software.

Determination of NADPH level

NADPH level were obtained via a NADP/NADPH assay kit (Abcam, ab65349) following the manufacturer's instructions. For the experiments, 4×10^4 iCtrl or *iXbp1* cells were plated out in opaque, white 96 well plates (Greiner, CELLSTAR, 655083), incubated for 24h in DMEM (10% FBS) and processed according to the manufacture's protocol. All measurements were performed as technical replicates (N = 3) and repeated as independent, biological experiments (n = 3) indicated in the respective figure legend.

Determination of GSH/GSSG ratio

GSH/GSSG ratios were obtained via a GSH/GSSG-GLO assay kit (Promega, V6611) following the manufacturer's instructions. For the experiments, 4×10^4 iCtrl or *iXbp1* cells were plated out in opaque, white 96 well plates (Greiner, CELLSTAR, 655083), incubated for 24h in DMEM (10% FBS) and processed according to the manufacture's protocol. GSH/GSSG ratios were determine by the following equation: total GSH-(GSSGx2)/GSSG. All measurements were performed as technical replicates (N = 3) and repeated as independent, biological experiments (n = 3) indicated in the respective figure legend.

Bioinformatic analysis of RNAseq and scRNAseq datasets

The publicly available datasets GSE109142, [47] (RNA sequencing TPM counts of pediatric ulcerative colitis patients) and GSE73661, [48] (microarray of UC patients treated with either infliximab or vedolizumab) were downloaded from the Gene Expression Omnibus (GEO) repository and processed using *R* version 4.2.2. TPM counts were log_2 transformed after adding a pseudo-count of 1 to remove zero values. If multiple microarray probe sets mapped to a same gene, the one exhibiting the highest variance was selected.

Digital gene expression matrices for SCP259[51] (colon mucosa of 18 UC patients and 12 healthy individuals) as well as the metadata file containing the annotated cell barcodes were downloaded from the Single Cell Portal and processed in *R* using the Seurat package.

Gene expression scores were calculated using the R package singscore (v1.18.0)[94,95] for the bulk datasets or as the mean of scaled lognormalised counts for the scRNA sequencing dataset. The ER stress signature was calculated on 62 ER stress related genes, as reported by Powell et al.[14] SSP score was calculated on the serine *de novo* synthesis pathway related genes *PHGDH*, *PSAT1* and *PSPH*. The cytoplasmic 1C cycle (CYTO) score was calculated on *MTHFD1*, *SHMT1* and *ALDH1L1* whereas *SHMT2, MTHFD2* and *ALDH1L2 was used for* the mitochondrial 1C cycle (MITO) score.

The differential gene expression analysis performed on a monolayer of microdissected epithelial cells isolated from 5 healthy control and 7 UC patients was downloaded from the editor's website.[49] For Figure 3A, RNAseq data from[46] were reanalyzed for TPM counts of *SLC7A11* and *ALDH1L2*.

Stable isotope tracing and metabolite extraction

Stable isotope tracing experiments were performed as previously described.[45] Briefly, [U-^{13}C]-glucose or [U-^{13}C]-glutamine (Cambridge Isotope Laboratories, CLM-1396 and CLM-1822) tracing was performed in DMEM supplemented with 10% FBS and the respective tracers (2 mM glutamine or 17 mM glucose). 2×10^5 cells were seeded in 12-well plates in triplicates for each experimental condition. Furthermore, an identical set of triplicate wells were plate-out to calculate the packed cell volume (PCV) by determining cell count and cell volume at the start and end of each tracing experiment.[37] After 24h, growth medium was replaced by ^{13}C tracer medium and cells were cultured for

an additional 24 h at 37°C. In parallel, starting PCV was determined by counting three wells per condition. To assess PCV at the end of the experiment, one set of triplicate wells was counted at the experimental endpoint, whereas another triplicates set was used for subsequent metabolite extraction. In addition, medium was collected, centrifuged at 350 g for 10 min at 4°C and supernatants were stored at −80°C until medium quantification via GC-MS or YSI.

For GC-MS analysis, cells from [U-^{13}C]-glucose and [U-^{13}C]-glutamine tracer experiments were washed once with 0.9% ice-cold NaCl. Thereafter, metabolites were extracted by adding 400 μL ice-cold MeOH/mqH$_2$O (ratio, 1:1) to each well. In addition, the extraction solvent contains the internal standards pentanedioc-d6 acid (CDN isotopologes, D5227) and [U-^{13}C]-ribitol (Omicron Biochemicals, ALD-062) at a final concentration of 1 μg/mL as well as Tridecanoid-d25 acid (CDN isotopologes, D4002) at a final concentration of 5 μg/mL. After the plates were incubated for 5 min at 4°C on a rocking shaker, supernatant was transferred to 1.5-mL Eppendorf tubes, mixed with 200 μL CHCl$_3$ (Merck, 650498), and centrifuged for 5 min at 13,000 g and at 4°C. Finally, the upper polar phase was collected, fully dried via SpeedVac and stored at −20°C for subsequent GC-MS analysis. For LC-MS analysis, metabolites extraction was performed as previously described[37] and extracted metabolites were stored at −80°C until LC-MS analysis.

GC-MS-based determination of MIDs of intracellular metabolites

Polar metabolites were derivatised for 90 min at 55°C with 20 μL of methoxyamine (c = 20 mg/mL) in pyridine under continuous shaking and subsequently for 60 min at 55°C with 20 μL of MTBSTFA w/1% TBDMCS. GC-MS analysis was performed using an Agilent 7890B GC coupled to an Agilent 5977A Mass Selective Detector (Agilent Technologies). A sample volume of 1 μL was injected into a Split/Splitless inlet, operating in splitless mode at 270°C. Gas chromatograph was equipped with a 30 m (I.D. 250 μm, film 0.25 μm) ZB-35MS capillary column with 5 m guard column (Phenomenex). Helium was used as carrier gas with a constant flow rate of 1.2 mL/min. GC oven temperature was held at 100°C for 2 min and increased to 300 °C at 10 °C/min and held for 4 min. Total run time was 26 min. Transfer line temperature was set to 280°C. Mass selective detector (MSD) was operating under electron ionisation at 70 eV. MS source was held at 230°C and the quadrupole at 150°C. For precise quantification of the MID, measurements were performed in selected ion monitoring mode. Target ions (m/z) and Dwell times are shown in Table S1.

The MetaboliteDetector software package (v. 3.220180913) was used for mass spectrometric data post processing, quantification, MID calculations, correction of natural isotope abundance, and determinations of fractional carbon contributions.[96]

Analysis of medium exchange rates

Medium quantification and exchange rate calculation was performed as described in.[37] For metabolite extraction, 20 μL of the collected medium sample was mixed with 180 μL extraction solvent (80% MeOH/20% mqH$_2$O) containing the internal standards [U-13C]-ribitol (50 μg/mL) and pentanedioc-d6 acid (20 μg/mL), vortexed for 10 s and subsequently incubated for 15 min at 4°C and 1350 rpm in a thermomixer. After centrifugation for 5 min at max speed, 50 μL of the supernatant was transferred in GC-vial and dried on SpeedVac overnight.

Metabolite derivatisation was performed by using a multi-purpose sample preparation robot (Gerstel). Dried medium extracts were dissolved in 30 μL pyridine, containing 20 mg/mL methoxyamine hydrochloride (Sigma-Aldrich), for 120 min at 45°C under shaking. After adding 30 μL N-methyl-N-trimethylsilyl-trifluoroacetamide (Macherey-Nagel), samples were incubated for 30 min at 45°C under continuous shaking.

GC-MS analysis was performed by using an Agilent 7890A GC coupled to an Agilent 5975C inert XL Mass Selective Detector (Agilent Technologies). A sample volume of 1 μL was injected into a Split/Splitless inlet, operating in split mode (10:1) at 270°C. The gas chromatograph was equipped with a 30 m (I.D. 0.25 mm, film 0.25 μm) DB-5ms capillary column (Agilent J&W GC Column) with 5 m guard column in front of the analytical column. Helium was used as carrier gas with a constant flow rate of 1.2 mL/min. The GC oven temperature was held at 90°C for 1 min and increased to 220 °C at 10 °C/min. Then, the temperature was increased to 280 °C at 20 °C/min followed by 5 min post run time at 325°C. The total run time was 22 min. The transfer line temperature was set to 280°C. The MSD was operating under electron ionisation at 70 eV. The MS source was held at 230°C and the quadrupole at 150°C. Mass spectra were acquired in selected ion monitoring (SIM) mode for precise quantification of medium components. In Table S2, masses used for quantification and qualification of the derivatised target analytes (dwell times between 25 and 70 ms) are illustrated.

All GC-MS chromatograms were processed using MetaboliteDetector (v. 3.2.20190704). Compounds were annotated by retention time and mass spectrum using an in-house mass spectral (SIM) library (overall similarity: >0.60). The following deconvolution settings were applied: Peak threshold: 2; Minimum peak height: 2; Bins per scan: 10; Deconvolution width: 8 scans; no baseline adjustment; Minimum 1 peaks per spectrum; no minimum required base peak intensity.

Peak areas of all isotopologues of defined quantification ions were summed up and divided by the peak area of the internal standard for normalisation. In addition, a calibration curve was prepared to calculate absolute concentrations. Absolute uptake and release rates were calculated as described previously.[96] In brief, the calibration curves were used to determine the absolute concentration of each analyzed metabolite in the samples as well as in the fresh medium. The absolute concentration of each metabolite in the sample was then substracted from the concentrations of the respective metabolites in the fresh medium. To calculate fmol/PCV/h, the obtained concentrations were then multiplied with the number of moles, divided by PCV and time of the experiment (24h) and subsequently multiplied by 1x10^{15}. Metabolite uptake is defined by negative values whereas positive values are related to metabolite release.

Formate release rates

Formate extraction, derivatisation and quantification was performed as described in.[45] In brief, a 1.5 mL tube containing 45 μL medium was supplemented with 20 μL of 1 mM internal standard (sodium $^{13}C,^2H$-formate (M+2), Sigma-Aldrich, CAS 1215684175), 10 μL of benzyl alcohol (Sigma-Aldrich, CAS 100516), 10 μL of 1 M sodium hydroxide, and 50 μL of pyridine. After 5 min on ice, derivatization was started under a fume hood by adding 20 μL of methyl chloroformate with vigorous vortexing for 20 s. Afterward, 200 μL H_2O and 100 μL of methyl tertiary butyl ether were added, and the sample was vortexed for another 20 s and centrifuged at 10,000g for 10 min at 10°C. 45 μL of the upper layer was transferred to a GC glass vial and stored at −80°C until analysis.

LC-MS measurements

Untargeted LC-MS analysis was carried out as previously.[37] The method was used to detect glutathione, cystine and γ-L-glutamyl-L-cysteine in cell extracts. For calculating intracellular metabolite level, measured peak areas were initially corrected for natural isotope abundance, normalised to internal standards and subsequently divided by PCV to obtain relative metabolite levels.

YSI measurements

Collected medium samples were initially filtrated (Phenex-RC 4mm Syringe Filters 0.2 μm) prior measurement to remove particles. Absolute quantitative values for glucose, lactate, glutamine and glutamic acid were acquired using the YSI 2950D Biochemistry Analyzer (Kreienbaum KWM). For a precise and reliable quantification, external calibration curves of each compound were prepared and measured in duplicates. To get absolute consumption and release rate (CORE, fmol/PCV/h), measured concentrations were divided by PCV (determined at start and end of the experiment, see stable isotope tracing for details) and the duration of the experiment.

Flow cytometric analysis of LPO levels

Image-iT Lipid Peroxidation Kit (Thermo Fisher Scientific, C10445) was used according to manufacturer's instructions. In brief, 250,000 iCtrl or *iXbp1* Mode-K cells were cultivated in 2 mL medium and treated after 24h as stated in the figure legends. Following 24h incubation, cells were harvest via trypsinization, centrifuged at 350 g for 5 min and washed with warm DMEM. Then, cells were stained in 100 μL DMEM supplemented with 10 μM Lipid peroxidation sensor (BODIPY 581/591 C11) for 30 min at 37°C. After two washing steps with ice-cold PBS at 350 g for 5 min, cells were resuspended in ice-cold 400 μL FACS buffer and measured using NovoCyte Quanteon system (Agilent). Data analysis was performed using FlowJo v10.6.2 software. All measurements were performed as independent, biological experiments (n ≥ 3).

Flow cytometric analysis of cytoplasmic ROS levels

250,000 iCtrl or *iXbp1* Mode-K cells were seeded in six-well plates and treated the subsequent day as indicated in the figure legends. After an incubation time of 24h, cells were stained with Zombie NIR (BioLegend, 1:1000 diluted in PBS) for 20 min at 37°C (to discriminate live and dead cells in the later analysis), detached with trypsin, centrifuged at 350 g for 5 min and washed with warm DMEM. Then, cells were stained in 100 μL DMEM supplemented with 10 μM DCF-DA (Sigma Aldrich, D6883) for 30 min at 37°C. After the incubation step, cells were centrifuged at 350 g for 5 min, washed twice with ice-cold PBS and resuspended in ice-cold FACS buffer (PBS with 10% FBS and 0.5 mM EDTA). Samples were measured using the BD FACSCanto system and BD FACSDiva software. Data analysis was performed using FlowJo v10.6.2 software. All measurements were performed as independent, biological experiments (n ≥ 3) indicated in the respective figure legend.

Western blot analysis

Cells and tissues were lysed using 40–100 μL SDS-based DLB buffer +1% Halt Protease inhibitor cocktail (Thermo Fisher Scientific, Waltham, USA) before incubation for 5 min at 95°C followed by sonication for 2 × 5 s. To remove cell remnants, lysates were centrifuged at 16.000 × g for 15 min at 4°C and supernatants were transferred into a new tube. For protein extraction of organoids, Matrigel (Corning, 356234) was removed by incubation of organoids in Corning Cell Recovery Solution (Corning, New York, USA) for 45–60 min on ice after transferring organoids to tubes, centrifugation at 3000g for 2 min and discarding supernatants. Next, the lysis buffer as described above was added. The protein concentration was determined applying the copper-based DC Protein Assay (Bio-Rad, Munich, Germany) according to the manufacturer's protocol. Proteins were separated by their molecular weight using precast gradient polyacrylamide gels for improved separation of a wide range of proteins (NuPAGE 4–12% Bis-Tris gels, Life Technologies, Darmstadt, Germany). Protein lysates were prepared by supplementation with the corresponding NuPAGE LDS Sample Buffer (Thermo Fisher Scientific, Bremen, Germany), followed by incubation at 70°C for 70 min. SDS-PAGE electrophoresis was run at 160 V and a maximum current of 300 mA for 1 to 2h in the XCell SureLock Mini Cell system (Life Technologies, Darmstadt, Germany). NuPAGE MOPS SDS running buffer (Thermo Fisher Scientific, NP0001) was used to run the gels and Prestained PageRuler plus protein ladder 10–250 K (Thermo Fisher Scientific, Bremen, Germany) served to estimate protein size. To detect proteins using immunodetection by specific antibodies, separated proteins were transferred onto polyvinylidene difluoride (PVDF) membranes. PVDF membranes (Bio-Rad, Munich, Germany) were activated under mild agitation using methanol for 10 s, followed by 5 min of washing in mqH₂O and then transferred for 5 min to anode buffer 1. Separated proteins were transferred from the gel onto the membrane by semi-dry blotting using the Trans-Blot Turbo Transfer System (Bio-Rad, Munich, Germany) with a discontinuous buffer system consisting of one cathode buffer and two anode buffers. Proteins were blotted onto the membrane at 0.3 A, 25 V for 60 min. After the transfer membranes were blocked with 5% (w/v) blotting grade blocker (non-fat dry milk, Bio –Rad, 1706404) in Tris-buffered saline (TBS) supplemented with 0.1%

(v/v) Tween 20 (TBS – T, Sigma Aldrich, P1379) for 1h. Membranes were probed with the appropriate primary and secondary antibody. The primary antibody was applied in 5% (w/v) blotting grade blocker (non-fat dry milk) or bovine serum albumin (BSA, Sigma Aldrich, A7030) in TBS-T according to the manufacturer's instruction and incubated overnight at 4°C under mild shaking. Next, the membrane was washed three times with TBS - T for 15 min to remove excess antibody. A horseradish peroxidase (HRP)-or IRDye-conjugated secondary antibody was diluted in 5% (w/v) blotting grade blocker (non-fat dry milk) in TBS-T according to the manufacturer's recommendation and incubated for 1h at room temperature. Binding of the secondary HRP-coupled antibody was detected using a chemiluminescent substrate kit (Thermo Fisher Scientific, 34580) and recorded with an automated developer machine (Agfa). Detection of IRDye-conjugated antibodies were recorded with an Odyssey imager system (Li-Cor Biosciences). The following antibodies were used: Actin β (Sigma-Aldrich, A-5441 or Cell Signaling Technology, 3700), β-Tubulin (MBL International, M150-3), Vinculin (Cell Signaling Technology, 13901), Aldh1l2 (Sigma-Aldrich, HPA039481), phospho-Sting (Cell Signaling Technology, 72971), phospho-Tbk1 (Cell Signaling Technology, 5483), Sting (Cell Signaling Technology, 13647), Tbk1 (Cell Signaling Technology, 38066), Lysozyme (Cell Signaling Technology, 60487), mouse-HRP (Amersham Biosciences, NA931V), rabbit-HRP (Amersham Biosciences, NA934V), rabbit-IRDye 800CW (Li-COR Technologies, 926–32213) and mouse- IRDye 680CW (Li-COR Technologies, 926–68070).

Quantitative real-time PCR (qRT-PCR) analysis

RNA extraction was performed using the RNeasy Mini Kit (Qiagen, Hilden, Germany) according to the manufacturer's instruction. To generate cDNA, 100-1000 ng total RNA (depending on the amount of previously extracted RNA) was transcribed into complementary DNA (cDNA) by reverse transcription using the Maxima H Minus First Strand cDNA Synthesis Kit (Thermo Fisher Scientific, Bremen, Germany) or the High-capacity cDNA Reverse Transcription Kit (Thermo Fisher Scientific, 4368814). Reverse transcription was performed following the manufacturer's instruction. qRT-PCR was used to amplify and simultaneously quantify mRNA levels using target-specific oligonucleotides. Predesigned TaqMan probes (Applied Biosystems, Carlsbad, USA were purchased and used. The 7900HT Fast Real-Time PCR System (Applied Biosystems, Darmstadt, Germany) was used for qRT-PCR experiments. Samples were run in duplicates on 384-well plates. For the PCR reaction, 5–10 ng cDNA and 0.5 μL of the respective TaqMan gene expression assays were used. The PCR program was carried out following the manufacturer's recommendation (TaqMan Gene Expression Master Mix protocol, Applied Biosystems, Darmstadt, Germany).

Alternatively, qRT-PCR was performed from 10 ng cDNA per sample using Fast SYBR Green Master Mix (Thermo Fisher Scientific, 4385612) at 95°C for 20 s, 40 cycles of 95°C for 1 s and 60°C for 20 s on the QuantStudio 5 Real-Time PCR System (Thermo Fisher Scientific). Relative quantification of each gene was done by QuantStudio Design&Analysis v1.5.1 software (Thermo Fisher Scientific) and comparative Ct method. All samples were analyzed in technical duplicates and repeated as independent, biological experiments (n ≥ 3). Moreover, all expression data were normalised to housekeeping genes (*Tbp*, *Hrpt1* or *Actinb*). Taqman assay probes were purchased from Life Technologies (*Cxcl10*, 04331182; *Gapdh*, 99999915; Ifnb1, 04331182; *Tmem173*, 04331182; *Xbp1*, 03464496) or Integrated DNA Technologies (*Shmt1* NM_009171(1); *Shmt2* NM_001252316(2); *Aldh1l1* NM_027406(1); *Aldh1l2* NM_153543(1); *Mthfd1* NM_138745(1); *Mthfd2* NM_008638(1); *Psat1* NM_001205339(2); *Psph* NM_133900(1); *Phghd* NM_016966(1) and *Actb* NM_007393(1)). All non-TaqMan assay mouse primers used in this study can be found in the Table S3.

QUANTIFICATION AND STATISTICAL ANALYSIS

GraphPad Prism 5 software package (GraphPad Software Inc., La Jolla, USA) was used for statistical analysis. If not otherwise specified, an unpaired, two-tailored Student's *t* test was performed. Data are visualised as mean $\pm$ standard error of the mean (SEM), if not otherwise stated. p values of <0.05 (*), <0.01 (**) or <0.001 (***) were considered statistically significant.

We define one *n* as one independent biological experiment (in some cases further consisting of several wells, e.g., triplicate wells for all stable isotope tracing experiments). The technical mean of one biological experiment was considered as one *n*. Mean values of several independent, biological experiments (as indicated in figure legends) were plotted and used for statistical analysis as indicated.